

Seasonal Variability of the Atlantic Meridional Overturning Circulation at 26.5°N

T. KANZOW,^{*,+} S. A. CUNNINGHAM,⁺ W. E. JOHNS,[#] J. J.-M. HIRSCHI,⁺ J. MAROTZKE,[@]
M. O. BARINGER,[&] C. S. MEINEN,[&] M. P. CHIDICHIMO,[@] C. ATKINSON,⁺ L. M. BEAL,[#]
H. L. BRYDEN,⁺ AND J. COLLINS^{**}

^{*} *Ozeanzirkulation und Klimadynamik, Leibniz-Institut für Meereswissenschaften an der Universität Kiel, Kiel, Germany*

⁺ *Ocean Observation and Climate Group, National Oceanography Centre Southampton, Southampton, United Kingdom*

[#] *Division of Meteorology and Physical Oceanography, Rosenstiel School of Marine and Atmospheric Science, Miami, Florida*

[@] *Ozean im Erdsystem, Max-Planck-Institut für Meteorologie, Hamburg, Germany*

[&] *Physical Oceanography Division, NOAA/Atlantic Oceanographic and Meteorological Laboratory, Miami, Florida*

^{**} *British Oceanographic Data Centre, Liverpool, United Kingdom*

(Manuscript received 19 August 2009, in final form 26 May 2010)

ABSTRACT

The Atlantic meridional overturning circulation (AMOC) makes the strongest oceanic contribution to the meridional redistribution of heat. Here, an observation-based, 48-month-long time series of the vertical structure and strength of the AMOC at 26.5°N is presented. From April 2004 to April 2008, the AMOC had a mean strength of 18.7 ± 2.1 Sv ($1\text{ Sv} \equiv 10^6 \text{ m}^3 \text{ s}^{-1}$) with fluctuations of 4.8 Sv rms. The best guess of the peak-to-peak amplitude of the AMOC seasonal cycle is 6.7 Sv, with a maximum strength in autumn and a minimum in spring. While seasonality in the AMOC was commonly thought to be dominated by the northward Ekman transport, this study reveals that fluctuations of the geostrophic midocean and Gulf Stream transports of 2.2 and 1.7 Sv rms, respectively, are substantially larger than those of the Ekman component (1.2 Sv rms). A simple model based on linear dynamics suggests that the seasonal cycle is dominated by wind stress curl forcing at the eastern boundary of the Atlantic. Seasonal geostrophic AMOC anomalies might represent an important and previously underestimated component of meridional transport and storage of heat in the subtropical North Atlantic. There is evidence that the seasonal cycle observed here is representative of much longer intervals. Previously, hydrographic snapshot estimates between 1957 and 2004 had suggested a long-term decline of the AMOC by 8 Sv. This study suggests that aliasing of seasonal AMOC anomalies might have accounted for a large part of the inferred slowdown.

1. Introduction

The Atlantic meridional overturning circulation (AMOC) plays a major role in the heat budget of the North Atlantic region. Hall and Bryden (1982) showed from observations that at 26°N the Atlantic circulation carries 1.3 ± 0.3 PW of heat northward, mostly within the AMOC. Their results were subsequently confirmed by global ocean inverse analyses (e.g., Ganachaud 2003b). The heat carried by the AMOC accounts for one-quarter of the maximum global meridional heat transport required by the coupled ocean–atmosphere system to balance the

global radiation budget. The Intergovernmental Panel on Climate Change considers it “very likely” that the AMOC will significantly weaken over the twenty-first century as a consequence of anthropogenic greenhouse gas emissions (Houghton et al. 2001), thus reducing the oceanic supply of heat to the North Atlantic region. Model simulations also suggest natural AMOC variability on intraseasonal to multidecadal time scales (e.g., Delworth et al. 1993; Jayne and Marotzke 2001; Latif et al. 2004; Biastoch et al. 2008; Wunsch and Heimbach 2009). A pronounced seasonal variability between the equator and midlatitudes reflects seasonally varying Ekman transports (e.g., Jayne and Marotzke 2001; Wunsch and Heimbach 2009). Multidecadal AMOC variability is thought to be linked to North Atlantic sea surface temperature changes (e.g., Delworth et al. 1993; Latif et al. 2004). However, owing to a lack of observations,

Corresponding author address: T. Kanzow, Ozeanzirkulation und Klimadynamik, Leibniz-Institut für Meereswissenschaften an der Universität Kiel, Düsternbrooker Weg 20, D-24105 Kiel, Germany.
E-mail: tkanzow@ifm-geomar.de

the existence of this link in the real ocean remains uncertain (Kanzow and Visbeck 2009).

The AMOC can be visualized as the meridional overturning streamfunction $\Psi(y, z, t)$ at any given latitude y by

$$\Psi(y, z, t) = \int_z^0 \int_{x_W}^{x_E} v(x, y, z, t) dx dz, \quad (1)$$

where $v(x, y, z, t)$ is the northward velocity with x , z , and t denoting the zonal, vertical, and time dimensions, respectively. The integration limits x_W and x_E stand for the zonal positions of the western and eastern boundaries of the Atlantic. Zonal hydrographic sections between 32°S and 56°N in the Atlantic suggest that Ψ consists of two (an upper and a lower) interhemispheric overturning cells (e.g., Talley et al. 2003), shown in Fig. 1. The upper cell is characterized by a northward flow that reaches down to 1300 m and a southward return flow of North Atlantic Deep Water (NADW) between 1300 and 4000 m. The overturning rate of the upper cell is estimated at 13–19 Sv ($1 \text{ Sv} \equiv 10^6 \text{ m}^3 \text{ s}^{-1}$), Fig. 1 (Ganachaud 2003b; Lumpkin and Speer 2007). The lower cell (Orsi et al. 2002) consists of northward flow of Antarctic Bottom Water (AABW) in the lower limb roughly below 5000 m (Fig. 1), with the transport diminishing northward due to entrainment of AABW into the overlying NADW, thereby requiring compensating southward NADW transport between 4000 and 5000 m (upper limb). At 26.5°N in the Atlantic the strength of the AABW cell amounts to $2 \pm 0.5 \text{ Sv}$ (Bryden et al. 2005b).

Daily estimates of the basinwide full-water-column-integrated AMOC became available when the U.K–U.S. Rapid Climate Change (RAPID)/meridional overturning circulation (MOC)/heat flux array (MOCHA) monitoring array (Kanzow et al. 2008a) (Fig. 2) across the Atlantic along 26.5°N became operational in April 2004. During the first year of array observations the AMOC had a mean strength of the upper cell of 18.7 Sv and an intraseasonal variability of 5.6 Sv rms (Cunningham et al. 2007).

In this study we describe seasonal AMOC transport variations as observed by the RAPID-MOC/MOCHA array at 26.5°N between April 2004 and April 2008. First, we present the dataset and the methodology underlying the computation of the strength and structure of the AMOC (section 2). We then discuss the temporal variability and vertical structure of the AMOC, with a focus on seasonal anomalies (section 3). In section 4 a forcing mechanism is proposed that accounts for a large fraction of the seasonal AMOC anomalies. Possible implications of our results are discussed in section 5. Conclusions are given in section 6.

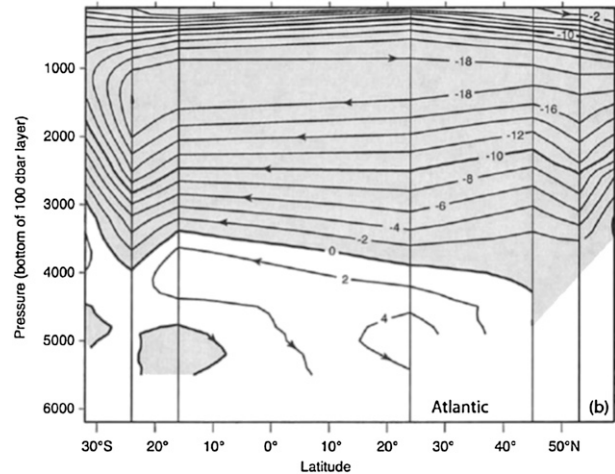


FIG. 1. Atlantic meridional overturning streamfunction $\Psi(y, z)$ from observations (from Talley et al. 2003), with a 2-Sv contour interval. The observations reveal two interhemispheric overturning cells, with the deep one involving AABW and the shallower one NADW.

2. Data and methods

a. Data

The three components of $\Psi(z)$ at 26.5°N are the Gulf Stream (T_{GS}), Ekman (T_{EK}), and midocean (T_{MO}) transports (Kanzow et al. 2007; Cunningham et al. 2007). The bulk of northward Gulf Stream volume transport, T_{GS} , has been monitored using a submarine cable and repeated ship sections nearly continuously since 1982 (Larsen 1992; Meinen et al. 2010). The vertical structure of $T_{GS}(z)$ is inferred from T_{GS} as described by Baringer et al. (2008).

The northward Ekman transport zonally integrated between the shelf of Abaco (Bahamas) and the African coast is estimated as the zonal integral of the zonal component of the wind stress from spaceborne Quick Scatterometer (QuikSCAT) measurements (Schlax et al. 2001). Then T_{EK} is assumed to be distributed evenly between the surface and 100 m, to obtain a vertical profile of transport per unit depth $T_{EK}(z)$.

For the midocean geostrophic transport T_{MO} , we use the RAPID-MOC/MOCHA moorings. To directly measure strong flows at the western boundary, moorings WB0–WB3 (Fig. 3) are equipped with current meters at discrete levels distributed throughout the water column, and at WBA and WB0 the velocity field in the upper 500 m is profiled by upward-looking acoustic Doppler current profilers (ADCPs) (Johns et al. 2008). All records are 40-h low-pass filtered, subsampled on a 12-hourly grid, and then interpolated onto a spatial grid of 0.5-km zonal and 20-m vertical resolution. Subsequently, profiles of zonally integrated transport (per unit depth) over the

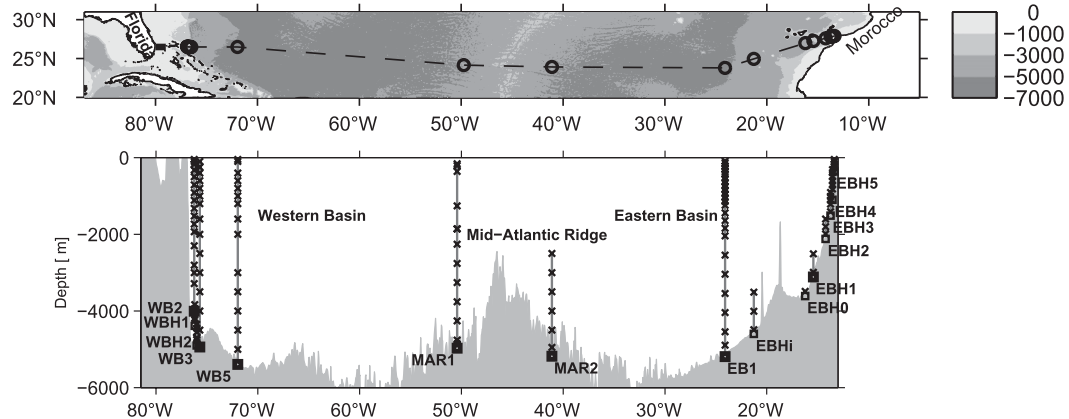


FIG. 2. (top) The distribution of moorings along 26.5°N in the subtropical North Atlantic. (bottom) Section of density (and bottom pressure) moorings along 26.5°N. The current meter moorings west of WB2 are not shown here for clarity (see Fig. 3).

16-km-wide western boundary wedge, $T_{WBW}(z)$, between the Abaco shelf and WB2 (Fig. 3) are computed (Johns et al. 2008).

The remainder of the midocean is measured by moorings near the western and eastern boundaries of the Atlantic and on both flanks of the mid-Atlantic ridge (MAR), which record temperature and salinity at discrete depths (Figs. 2a,b). These records are calibrated and subsequently 2-day low-pass filtered and subsampled at 12-hourly resolution (Kanzow et al. 2006, 2007). At the eastern boundary temperature and salinity data from several moorings have been merged into one profile from 4840 m to the shallowest available level during each deployment (Kanzow et al. 2007, 2009). The western boundary end-of-section profile uses data merged from WB2 shallower than 4000 m and from WBH1/WBH2 (or WB3 after April 2005) at depths greater than that (Fig. 2b). At the western flank of the MAR mooring, MAR1 provides temperature and salinity from the sea surface to 5000 m; on the eastern flank, MAR2 covers the 2500–5000-m interval (Fig. 2b). Filtered and subsampled temperature and salinity data at each site are vertically interpolated onto a 20-dbar grid (Kanzow et al. 2007), from which densities ρ are then computed. Vertical profiles of density at the western and eastern boundaries (ρ_w , ρ_e) and on the western and eastern flanks of the mid-Atlantic ridge (ρ_{MARW} , ρ_{MARE}) are used to compute zonally basinwide-integrated northward geostrophic internal transport per-unit-depth $T_{INT}(z)$ relative to a deep reference level $z_{REF} = -4740$ m (appendix A). Northward transports of AABW at depths greater than 5000 m are accounted for by extending the transport profile to 6000 m using historical estimates (appendix A). Here $T_{INT}(z)$ and $T_{WBW}(z)$ are used to compute the midocean geostrophic transport (section 2b).

b. Methodology

Since each variable in this study is a function of t , the explicit mentioning of the time dependence will be dropped hereafter. Throughout this study, then, $T_{GS}(z)$, $T_{EK}(z)$, $T_{MO}(z)$, and so on will indicate profiles of transport per unit depth (Sv m^{-1}), whereas T_{GS} , T_{EK} , T_{MO} , etc. will represent transports (Sv) integrated over a vertical range.

At each time step, the strength of the AMOC, Ψ^{MAX} , will be defined as the maximum of the overturning streamfunction $\Psi(z, t)$ (or maximum northward upper-ocean transport), according to

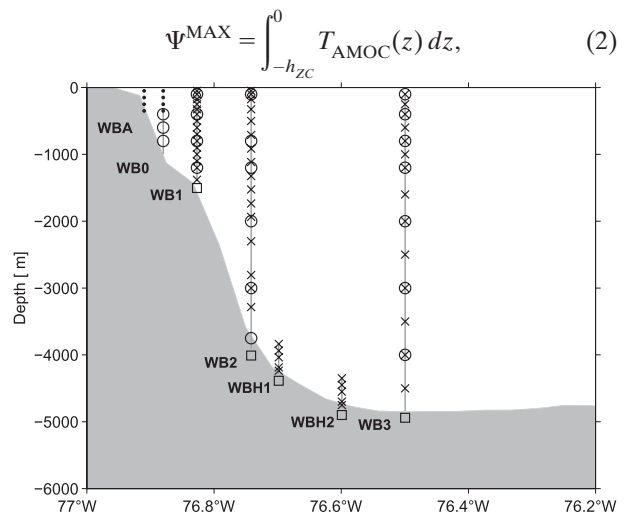


FIG. 3. Moorings near the western boundary (off Abaco, the Bahamas): density sensors (crosses), bottom pressure recorders (squares), and current meters (circles). The dots at WBA and WB0 indicate the part of the water column covered by ADCP measurements. WBH1 and WBH2 were only deployed during the period from April 2004 to 2005.

where $h_{ZC}(t)$ represents the depth of the lower boundary of the upper-ocean northward-flowing branch of the AMOC (Fig. 1) and $T_{AMOC}(z)$ is the vertical profile of zonally integrated northward transport per unit depth—that is, the sum of components $T_{EK}(z)$, $T_{GS}(z)$, and $T_{MO}(z)$ (Kanzow et al. 2009). Hence, before we can calculate Ψ^{MAX} , we need to estimate $T_{MO}(z)$, which consists of two components: (i) $T_{WBW}(z)$ and (ii) the *absolute* transport between WB2 and the eastern boundary (Fig. 2). For (ii), a time-variable reference transport for the relative $T_{INT}(z)$ needs to be provided. This is achieved by the imposition of a precise compensation among the different flow components, in the sense that the sea surface to sea floor integral of $T_{AMOC}(z)$ yields zero residual mass transport across 26.5°N at each time step, according to

$$\int_{-h_{BOT}}^0 T_{AMOC}(z) dz = \int_{-h_{BOT}}^0 [T_{GS}(z) + T_{EK}(z) + T_{MO}(z)] dz = 0. \quad (3)$$

Kanzow et al. (2007) showed observational evidence for an approximate compensation among the different transport components in (3) over periods in excess of 10 days, using independent bottom pressure measurements. At time scales shorter than 10 days, there are pronounced net barotropic transport fluctuations of ± 8 Sv across 26.5°N (see Fig. 2a of Kanzow et al. 2007), which are possibly related to large-scale atmospheric pressure forcing (Bryden et al. 2009). Notable density fluctuations largely compensating for barotropic transports are found at periods in excess of 10 days (Kanzow et al. 2007).

The referencing of $T_{INT}(z)$ is carried out by computing a compensating transport T_C at each time step as follows

$$T_C = - \int_{-h_{BOT}}^0 [T_{GS}(z) + T_{EK}(z) + T_{WBW}(z) + T_{INT}(z)] dz. \quad (4)$$

It is assumed that the compensating meridional velocity field $V_C(x, z)$ underlying T_C is spatially uniform both in the vertical and zonal domains following model simulations of Hirschi et al. (2003) and Hirschi and Marotzke (2007). Accordingly, $T_C(z) = V_C L(z)$, with L denoting the effective zonal width of the ocean, which decreases with depth. Hence, the absolute midocean transport $T_{MO}(z)$ can be calculated as

$$T_{MO}(z) = [T_{INT}(z) + T_C(z) + T_{WBW}(z)]. \quad (5)$$

Last, the *upper* midocean transport T_{UMO} constitutes that part of $T_{MO}(z)$ that contributes to Ψ^{MAX} as follows:

$$T_{UMO} = \int_{-h_{ZC}}^0 T_{MO}(z) dz. \quad (6)$$

We now limit our analysis and discussion to 10-day low-pass filtered transports; however, three main factors may allow for nonzero net mass fluxes across 26.5°N at periods longer than 10 days, namely, regional mass storage, external mass sources (net precipitation), and the Arctic throughflow (Bering Strait). The significance of mass storage can be inferred indirectly from bottom pressure measurements. At 26.5°N we observe peak-to-peak bottom pressure fluctuations of 0.04 and 0.05 dbar at time scales of 20 and 180 days that exhibit basinwide correlation scales. If the Atlantic north of 26.5°N displays coherent mass changes, this would correspond to uncompensated meridional transports of 0.5 and 0.1 Sv on 20-day and 180-day scales, respectively. For the second two factors, the southward mass transport associated with the Bering Strait flow plus net precipitation between the Bering Strait and 26.5°N is thought to vary in time by less than 1 Sv on intraseasonal time scales (Woodgate and Aagaard 2005; Wijffels 2001). Hence, we assume that the net mass (i.e., uncompensated) transport across 26.5°N could be 1.0 Sv rms on 20-day time scales, decreasing to less than 0.5 Sv rms on seasonal time scales. A mass imbalance of 1.0 Sv rms produces an error in the inferred Ψ^{MAX} of 0.2 Sv rms (appendix B). As we will show later, the fluctuations of Ψ^{MAX} are much larger than this.

c. Isolation of the different transport contributions to the AMOC

It is useful to isolate the contribution of the western and eastern boundaries of the midocean section to fluctuations in Ψ^{MAX} , so that physical mechanisms of density changes at either boundary can be studied separately (Longworth 2007). For this, $\overline{T}_{GS}(z)$ and $\overline{T}_{EK}(z)$ are fixed in (3) and (4) by using 4-yr-average profiles. In addition, to isolate the western boundary contribution to the overturning Ψ_{MOW}^{MAX} (i.e., from the continental slope east of the Bahamas), 4-yr-average density profiles $\overline{\rho}_E(z)$, $\overline{\rho}_{MAR1}(z)$, and $\overline{\rho}_{MAR2}(z)$ are used for the computation of $T_{INT}(z)$ in (A1), (A3), (A4), so that the only contributions to Ψ_{MOW}^{MAX} that vary in time are $T_{WBW}(z)$ and $\rho_W(z)$. Similarly, to isolate the eastern boundary contribution to the time-variable overturning Ψ_{MOE}^{MAX} , 4-yr-average density profiles $\overline{\rho}_W(z)$, $\overline{\rho}_{MAR1}(z)$, and $\overline{\rho}_{MAR2}(z)$ are used for the computation of $T_{INT}(z)$ in (A1), (A3), (A4), so that the only time-variable contribution comes from $\rho_E(z)$. To isolate the overturning transport resulting from the sum of all western boundary transport contributions—hereafter referred to as Ψ_W^{MAX} —the time-variable profiles of

$T_{\text{WBW}}(z)$ and $\rho_W(z)$ and $T_{\text{GS}}(z)$ are used together with the time-average profiles of $\bar{T}_{\text{EK}}(z)\bar{\rho}_E(z)$, $\bar{\rho}_{\text{MAR1}}(z)$, and $\bar{\rho}_{\text{MAR2}}(z)$ in the calculations [(3), (4), (A1), (A3), (A4)].

3. Results

a. Vertical structure of the flow field across 26.5°N

The April 2004–08 mean profile of $T_{\text{AMOC}}(z)$ exhibits northward flow between the surface and 1025 m (Fig. 4), which is a combination of the northward transport of 31.7 ± 0.9 Sv of T_{GS} shallower than 780 m (Beal et al. 2008), 3.5 ± 0.8 Sv of T_{EK} shallower than 100 m, and 0.9 ± 0.2 Sv of T_{MO} (dashed line) in the Antarctic Intermediate Water (AAIW) range between 660 and 1025 m. The bulk of northward flows are opposed by 17.5 ± 1.4 Sv of southward flow of T_{MO} shallower than 660 m (Fig. 4a), with the latter mostly accounting for the recirculation within the subtropical gyre but also containing roughly 5 Sv of northward and western boundary flow within the Antilles Current (Bryden et al. 2005a). Each of the above error envelopes represents the sum of the standard error (SE) and the expected measurement error (appendix B).

There is 20.7 ± 1.9 Sv of southward flow of NADW between 1025 and 5200 (Fig. 4b). In this layer maximum southward transports are found near 1700 m. A time-mean northward transport of 2.1 Sv (appendix A) at depths larger than 5000 m is prescribed, to approximately account for the unobserved AABW flow (Bryden et al. 2005b), which translates in an uncertainty in the time mean Ψ^{MAX} of less than ± 0.2 Sv (appendix B). Thus, the imposition of a constant AABW transport will only have a small effect on Ψ^{MAX} .

Figure 5 shows snapshots every 5 days of the meridional overturning streamfunction $\Psi(z)$ at 26.5°N (1). The time-mean Ψ^{MAX} is 18.7 ± 2.1 Sv, with an average zero-crossing depth h_{ZC} at 1025 m, varying by 125-m rms. Note that this result illustrates why a “level of no motion” assumption associated with the mean depth of a property interface such as the AAIW–NADW interface is potentially inaccurate (Figs. 5 and 6a).

b. Time-variable meridional flow

Figure 7 shows time series of Ψ^{MAX} at 26.5°N and its components. The Ψ^{MAX} varies by 4.8 Sv rms (red line), and both it and its components display pronounced intra-seasonal and seasonal variability; T_{GS} varies by 2.9 Sv rms, a value representative of the full 1982–2008 record of continuous cable measurements (Meinen et al. 2010) (Table 1); T_{EK} fluctuates by 3.5 Sv rms and is also representative of longer observational periods (Table 1) (Kalnay et al. 1996); T_{UMO} , representing the vertical

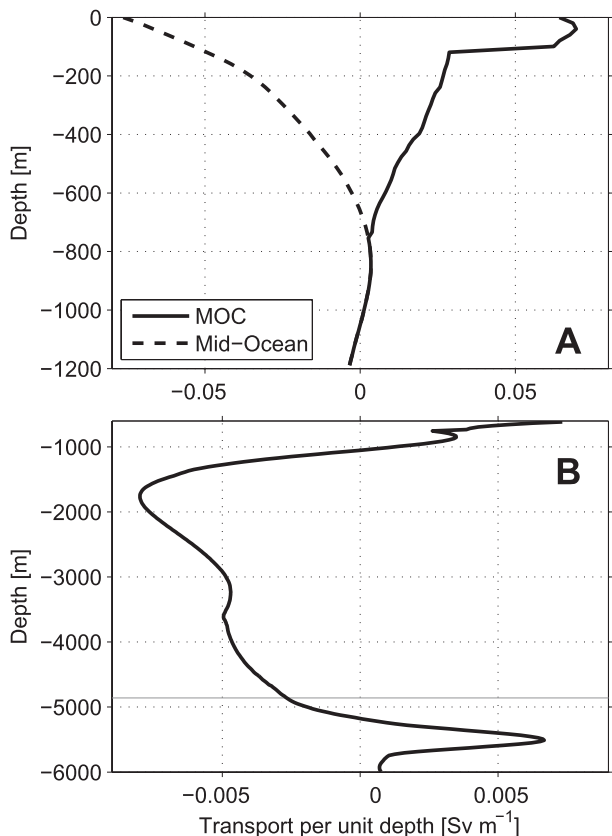


FIG. 4. Zonally integrated northward transport (Sv m^{-1}) across 26.5°N (top) shallower than 1000 m and (bottom) deeper than 600 m. The bold solid line represents the April 2004–April 2008 time mean of $T_{\text{AMOC}}(z)$; the dashed line is the time mean of $T_{\text{MO}}(z)$. The abyssal transport structure (below the gray line) is estimated based on the synthetic approximation to historical estimates from Fig. A1.

integral of $T_{\text{MO}}(z)$ between the surface and h_{ZC} [Fig. 6a, Eq. (6)], displays fluctuations of 3.2 Sv rms. Since no continuous observations of T_{UMO} were made prior to April 2004, the representativeness of this result can only be assessed indirectly (section 5). The correlations for the transport pairs $\langle T_{\text{EK}}, T_{\text{GS}} \rangle$, $\langle T_{\text{EK}}, T_{\text{UMO}} \rangle$, and $\langle T_{\text{GS}}, T_{\text{UMO}} \rangle$ (0.01, -0.11, and -0.21, respectively) are insignificant at 10% error probability, and hence each of them projects on the variance of Ψ^{MAX} . The correlations for the transport pairs $\langle \Psi^{\text{MAX}}, T_{\text{GS}} \rangle$, $\langle \Psi^{\text{MAX}}, T_{\text{UMO}} \rangle$, and $\langle \Psi^{\text{MAX}}, T_{\text{EK}} \rangle$ are 0.42, 0.43, and 0.62, respectively, and are all significant at 5% error probability. Although T_{EK} , T_{GS} , and T_{UMO} vary by roughly the same amount, their frequency distribution displays remarkable differences (Fig. 8). The ageostrophic T_{EK} dominates fluctuations of Ψ^{MAX} at periods between 10 and 90 days, while the seasonal variability of Ψ^{MAX} is dominated by geostrophic (density balanced) components T_{UMO} and T_{GS} . The contribution to Ψ^{MAX} from the compensation transport $T_C(z)$

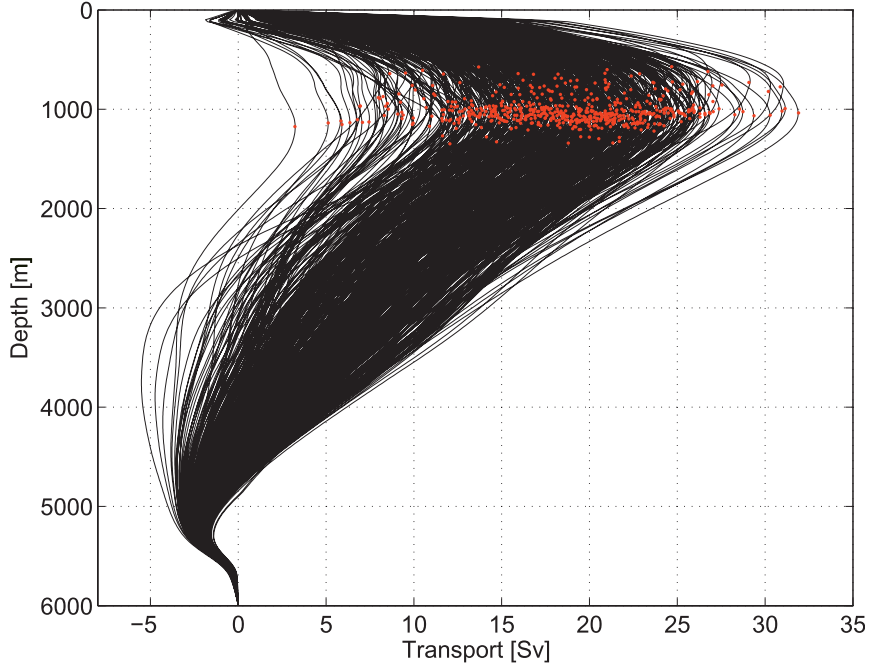


FIG. 5. Overturning streamfunction $\Psi(z) = \int_z^0 T_{\text{AMOC}}(z') dz$ at 26.5°N , based on 10-day low-pass filtered $T_{\text{AMOC}}(z)$. One profile every five days has been plotted over the 48-month-long measurement period between April 2004 and April 2008. The red dots on each profile mark the maximum northward transport Ψ^{MAX} and the corresponding depth h_c .

at depths shallower than h_{ZC} (gray line in Fig. 7) is ± 2.3 Sv, somewhat less than the variability of T_{UMO} , T_{GS} , or T_{EK} . As T_C compensates for fluctuations in T_{GS} , T_{EK} , and in the observed components of T_{UMO} [i.e., T_{INT} and T_{WBW} ; see (5)], it is negatively correlated to all of them (-0.28 , -0.41 , and -0.42 , respectively).

On seasonal time scales, the 180-day low-pass filtered time series of T_{UMO} , T_{GS} , and T_{EK} display fluctuations of 2.2, 1.7, and 1.3 Sv rms, respectively. The sum of the *geostrophic upper-ocean transports* that contribute to Ψ^{MAX} (i.e., T_{UMO} plus T_{GS}) varies by 2.7 Sv rms and clearly dominates over T_{EK} . Moreover, Fig. 8 shows that this result is robust over a 26-yr time series of T_{GS} and T_{EK} (dashed blue and black lines in Fig. 8).

The separate contributions to Ψ^{MAX} from the western and eastern boundary variability of the midocean section to $\Psi_{\text{MOW}}^{\text{MAX}}$ and $\Psi_{\text{MOE}}^{\text{MAX}}$ (see section 2c) fluctuate by 2.3 and 2.1 Sv rms, respectively (Fig. 9, black and gray lines), and are uncorrelated at 10% error probability. The contribution to Ψ^{MAX} from the western boundary, including the Gulf Stream Ψ_W^{MAX} (section 2c), fluctuates by 3.0 Sv rms (not shown) and thus exceeds the variability of $\Psi_{\text{MOE}}^{\text{MAX}}$. There is a similar picture at seasonal periods (180-day low-pass filtered records), with Ψ_W^{MAX} , $\Psi_{\text{MOW}}^{\text{MAX}}$, and $\Psi_{\text{MOE}}^{\text{MAX}}$ yielding values of 2.0, 1.4, and 1.3 Sv rms, respectively.

c. Seasonal cycle

Does the Ψ^{MAX} or any of the three upper-ocean contributions exhibit a well-developed seasonal cycle? If so, a prediction of Ψ^{MAX} , and of its role in ocean heat storage and meridional heat transport on seasonal time scales might be possible, provided the physics of the forcing are understood. The seasonal cycle of T_{GS} is shown as black solid lines in Fig. 10a (Meinen et al. 2010) and has an amplitude of 3.0 Sv peak to peak with a maximum in July and a minimum in November. After 4 years of measurements the seasonal cycle stands out weakly from the mean monthly standard error of ± 1.1 Sv [i.e., the mean monthly standard deviation (std dev) divided by $\sqrt{4}$; Table 1]; however, both amplitude and phase are consistent with the seasonal cycle computed from the 26-yr-long time series (dashed line in Fig. 10a).

The seasonal cycle of T_{EK} (Fig. 10b, solid line) has an amplitude of 4.1 Sv peak to peak with a maximum in December and a minimum in March (average standard error ± 0.8 Sv). However, monthwise averages do not bring out a seasonal periodicity in T_{EK} (Böning et al. 2001), and the seasonal “cycle” derived from the 4-yr record is not representative of the 26-yr-long record (dashed line in Fig. 10b), which exhibits 2.1 Sv peak to peak with a minimum in June and maximum in January.

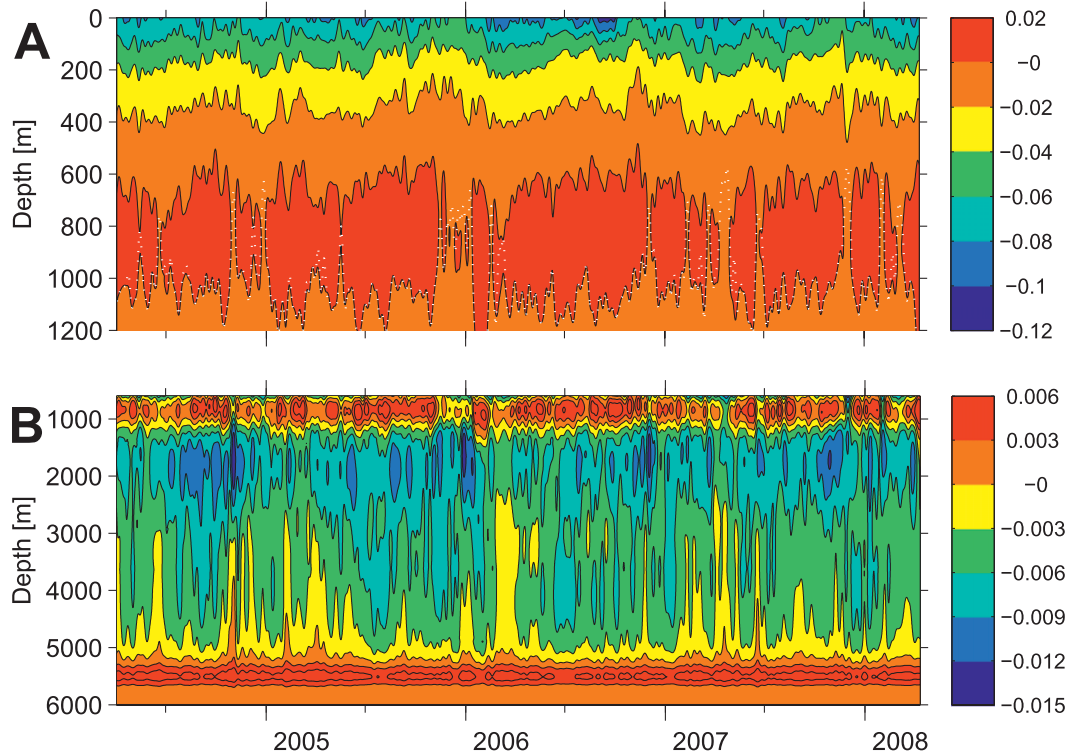


FIG. 6. Midocean transport (Sv m^{-1}) $T_{\text{MO}}(z)$ (a) shallower than 1200 m and (b) deeper than 600 m (note that the two panels overlap in the 600–1200-m depth range). The data are 10-day low-pass filtered. Note that the transport scale in (a) is much broader than in (b). The interface depth between the upper and lower branches of the upper (NADW) overturning cell h_{ZC} is shown as a white dotted line.

While phase and amplitude of the maximum transport obtained from the long record and the short record are in agreement, the March minimum of the 4-yr record is dominated and biased by unusually strong southward flow in March 2005 (Atkinson et al. 2008).

The T_{UMO} shows a seasonal cycle of 5.9 Sv peak to peak, with a minimum northward transport in April and a maximum one in November (Fig. 10c), clearly significant above the mean monthly standard error of ± 1.0 Sv. The seasonal cycle of T_{UMO} is clearly stronger than that of T_{GS} and T_{EK} . The seasonal variability of the vertical profile associated with T_{UMO} is illustrated in Fig. 11, where monthly-mean profiles of the $T_{\text{MO}}(z)$ anomaly are shown. The maximum northward flow anomaly occurs in the upper ocean in November and the minimum (relative southward) anomaly occurs in April, consistent with the seasonal cycle of T_{UMO} . Below roughly 1000 m, the pattern is of opposite sign, and the overall variability can therefore be described fundamentally as a first-modelike internal variation of the basinwide, zonally averaged interior flow.

Overall, Ψ^{MAX} exhibits a variability of 7.8 Sv peak to peak, with minimum northward transport in March and maxima in July and November (solid line in Fig. 10d).

However, this seasonal cycle of Ψ^{MAX} is contaminated by the bias in T_{EK} (Fig. 10b): we can derive a better estimate using the long-term seasonal cycles of the components $T_{\text{EK}}^{\text{cycle26y}}$ and $T_{\text{GS}}^{\text{cycle26y}}$ (dashed lines in Figs. 10a,b). Recall, there is no long-term estimate of T_{UMO} , only $T_{\text{UMO}}^{\text{cycle4y}}$; however, this is also contaminated by T_{EK} through the compensation transport T_c , roughly 25% of which takes place in the upper 1000 m (Fig. 4). By replacement of the compensation for $T_{\text{EK}}^{\text{cycle4y}}$ and $T_{\text{GS}}^{\text{cycle4y}}$ (i.e., 25% of the amplitude) by a compensation for the long-term seasonal cycles ($T_{\text{EK}}^{\text{cycle26y}}$, $T_{\text{GS}}^{\text{cycle26y}}$), this contamination can be removed. Accordingly, the long-term seasonal cycle of Ψ^{MAX} is estimated by

$$\begin{aligned} \Psi^{\text{cycle}} = & T_{\text{UMO}}^{\text{cycle4y}} + 0.75 \times [T_{\text{GS}}^{\text{cycle26y}} + T_{\text{EK}}^{\text{cycle26y}}] + 0.25 \\ & \times [T_{\text{GS}}^{\text{cycle4y}} + T_{\text{EK}}^{\text{cycle4y}}], \end{aligned} \quad (7)$$

which has an amplitude of 6.7 Sv peak to peak with a minimum in March and maxima in July and November (Fig. 10d); the standard error is ± 1.2 Sv. The best estimates of the long-term seasonal cycles have been superimposed on the 4-yr-long transport time series (Fig. 7). For Ψ^{MAX} and T_{UMO} the corresponding seasonal cycles

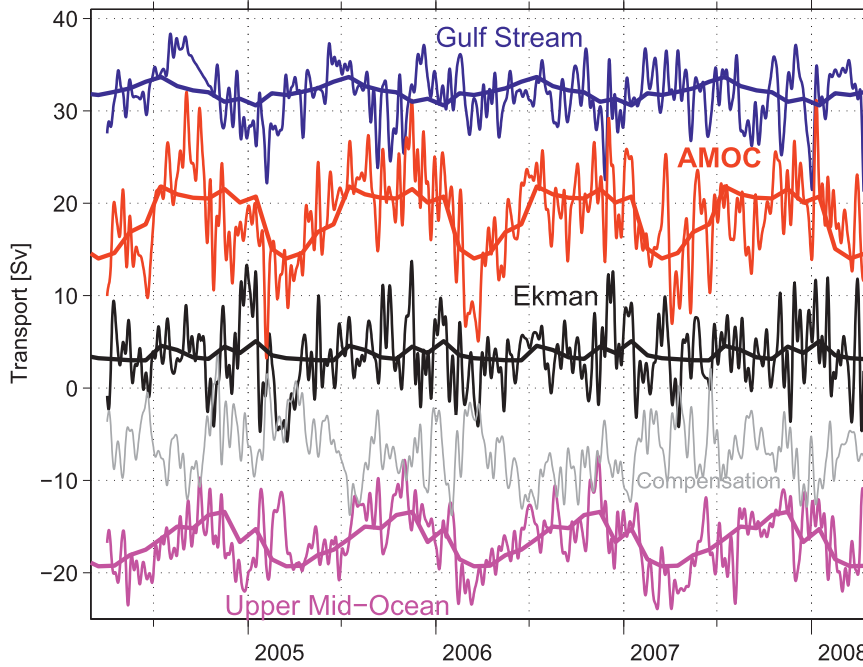


FIG. 7. The thin lines denote the time series of Ψ^{MAX} (red), T_{GS} (blue), T_{EK} (black), and T_{UIMO} (magenta) for the period between April 2004 and April 2008. The data have been 10-day low-pass filtered. Also shown is the contribution of the compensation transport to Ψ^{MAX} [i.e., $T_C(z)$] integrated between the sea surface and the level of no motion]. The bold lines represent the best estimates of the long-term seasonal cycles of each transport component (see section 3c and Fig. 10).

account for a large fraction of the variance, while this is not the case for T_{EK} and T_{GS} .

Figure 12 displays the contributions to Ψ^{cycle} from the western and eastern boundary fluctuations of the mid-ocean section (as shown in Fig. 9). The western boundary signal $\Psi_{\text{MOW}}^{\text{MAX}}$ (Fig. 12a) has a smaller seasonal cycle with larger uncertainties than the eastern boundary one, $\Psi_{\text{MOE}}^{\text{MAX}}$ (Fig. 12b) (3.9 versus 5.4 Sv peak to peak, with standard errors of 1.0 versus 0.5 Sv). Thus, the eastern boundary variability (with a transport minimum in April and maximum in October) dominates the seasonal cycle of T_{UIMO} . Chidichimo et al. (2010) also find a coherent seasonal cycle in thermocline eastern margin densities at 26.5°N.

4. Causes of midocean seasonal transport cycle

The variability in T_{UIMO} is geostrophic and, therefore, its seasonal cycle is directly related to the difference in seasonal density anomalies between the eastern and western boundaries. Above we found that the eastern boundary density variability dominates over the western boundary (Fig. 12) and that the seasonal signal in T_{UIMO} extends to 1000-m depth (Fig. 11). The latter suggests that the seasonal cycle is not fundamentally related to buoyancy forcing at the ocean surface, but is likely a dynamical response to seasonal wind forcing. Next, we consider

a simple model of the forced response of the ocean interior to seasonal wind stress curl variations, focusing on the baroclinic response, to try to attribute a mechanism to the observations.

The linear, subinertial response of a stratified ocean to wind stress curl variability can be expressed in terms of vertical modes $\Phi_n(z)$, whose time and zonally varying amplitude $p_n(x, t)$ is given by (Anderson and Gill 1975; Sturges et al. 1998)

$$\frac{\partial p_n}{\partial t} - \beta c_n^2 f^{-2} \frac{\partial p_n}{\partial x} = -c_n^2 f^{-1} G_n \nabla \times \tau, \quad (8)$$

where β is the planetary vorticity gradient ($\partial f / \partial y$), c_n is the long Rossby wave speed for the n th vertical mode, and G_n is an amplitude factor governing the projection of the forcing onto the vertical modes:

$$G_n = H_{\text{mix}}^{-1} \int_{-H_{\text{MIX}}}^0 \Phi_n(z) dz \left/ \int_{-H}^0 \Phi_n(z)^2 dz \right., \quad (9)$$

where H_{mix} is the mixed layer depth.

We calculated vertical modes $\Phi_n(z)$ and the associated c_n from climatological (Levitus 1982) hydrographic data along 26.5°N and chose the results from a representative longitude (60°W) for the calculation. Equation (8) was

TABLE 1. Basic statistics of the different transport components (Sv) discussed in this study for the period between April 2004 and April 2008 (the values in brackets in columns 2 and 4 refer to the period between October 1982 and January 2008) based on 10-day low-pass filtered data. The standard error (SE) in column 4 represents the average of the 12 monthly standard errors. The integral time scale of the 4-yr-long time series in column 4 has been computed according to appendix B. The asterisk indicates calculations based on (7).

Component	Mean/std dev Apr 2004–Oct 2007 (Oct 1982–Jan 2008)	Integral time scale (days)/DOF	Seasonal cycle min (mm)/max (mm)/SE Apr 2004–08 (Oct 1982–Jan 2008)
T_{GS}	31.7/2.9 (32.1/3.1)	29/51	30.5 (Nov)/33.4 (Jul) 1.1 [30.6 (Jan)/33.6 (Jul)]
T_{EK}	3.5/3.5 3.7/3.1	12/121	1.5 (Mar)/5.6 (Dec)/0.8 [3.0 (Jun)/5.1 (Jan)]
T_{UMO}	-16.5/3.2 (N/A)	47/32	-19.3 (Apr)/-13.4 (Nov)/0.9 (N/A)
Ψ^{MAX}	18.7/4.8 (N/A)	46/32	14.0 (Mar)/21.8 (Jul)/1.4 [14.8 (Mar)/21.5 (Jul)]*
Ψ_{MOW}^{MAX}	18.7/3.0 (N/A)	40/37	17.6 (Feb)/21.2 (Aug)/1.2 (N/A)
Ψ_{MOW}^{MAX}	18.7/2.3 (N/A)	34/43	16.9 (Feb)/20.8 (Aug)/0.9 (N/A)
Ψ_{MOE}^{MAX}	18.7/2.1 (N/A)	43/34	16.6 (Apr)/22.0 (Oct)/0.5 (N/A)

solved in a forward time-stepping mode from zero initial conditions using the climatological seasonal cycle of wind stress curl anomaly across 26.5°N (Fig. 13a) extracted from the Scatterometer Climatology of Ocean Winds

(SCOW) (Risien and Chelton 2008). The equilibrium seasonal cycle of p_n across the basin then results in a basinwide midocean geostrophic transport anomaly for each mode of

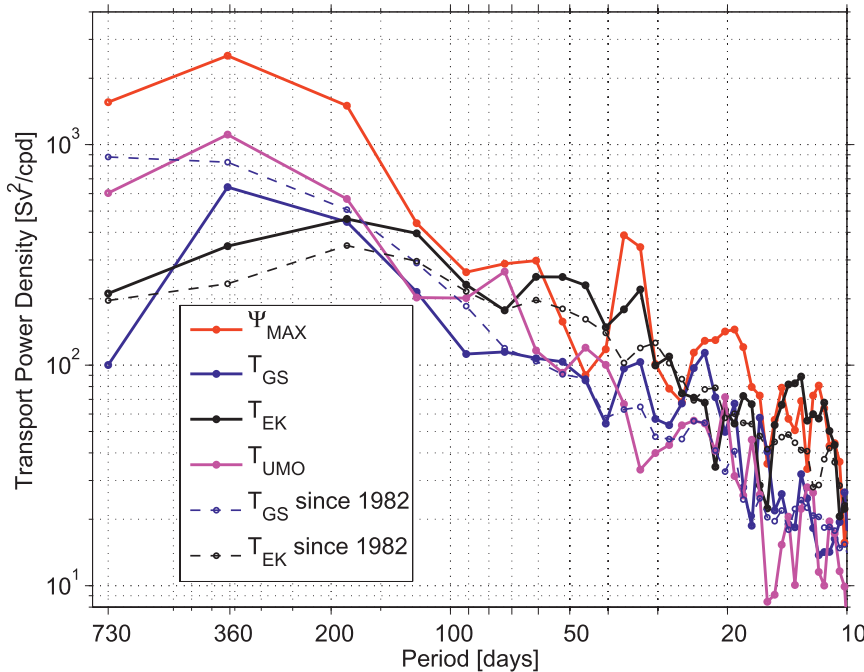


FIG. 8. Solid lines denote power spectra of Ψ^{MAX} (red), T_{GS} (blue), T_{EK} (black), and T_{UMO} (magenta) for the period from April 2004 to April 2008 (as shown in Fig. 7). Also shown for reference purposes as dashed lines are the transport spectra of T_{GS} (blue) and T_{EK} (black) based on time series between March 1982 and January 2008. The long T_{EK} time series is based on NCEP–NCAR reanalysis data (Kalnay et al. 1996). The spectra are based on Welch's periodogram method using a 365 (730)-days-wide Hamming window and 182 (365) days' overlap between consecutive data segments for periods $\leq (>) 365$ days.

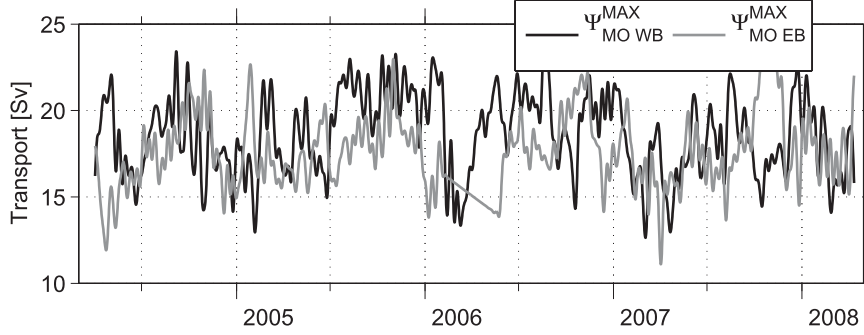


FIG. 9. Ten-day low-pass filtered time series of the western ($\Psi_{\text{MO WB}}^{\text{MAX}}$, black line) and eastern ($\Psi_{\text{MO EB}}^{\text{MAX}}$, gray line) boundary contributions of the midocean section to the overturning strength (see section 2c for details). For the computation, T_{GS} and T_{EK} have been prescribed as time invariant.

$$\begin{aligned} T_{\text{MO}_n}^{\text{V}\times\tau}(z) &= \int_{X_W}^{X_E} v_n(z) dx = \int_{X_W}^{X_E} (\rho f)^{-1} \frac{\partial p_n}{\partial x} \Phi_n(z) dx \\ &= (\rho f)^{-1} \Phi_n(z) [p_n(x_E) - p_n(x_W)]. \end{aligned} \quad (10)$$

The seasonal cycle of $p_n(x_E)$ is given simply by the locally forced solution at the eastern boundary. The western

boundary signal $p_n(x_W)$ represents the locally forced solution at the western boundary plus accumulated effects of Rossby wave propagation from forcing west of the mid-Atlantic ridge at 50°W since studies indicate that the MAR effectively blocks propagation of baroclinic Rossby waves from the eastern basin (Barnier 1988; Herrmann and Krauss 1989; Osychny and Cornillon 2004).

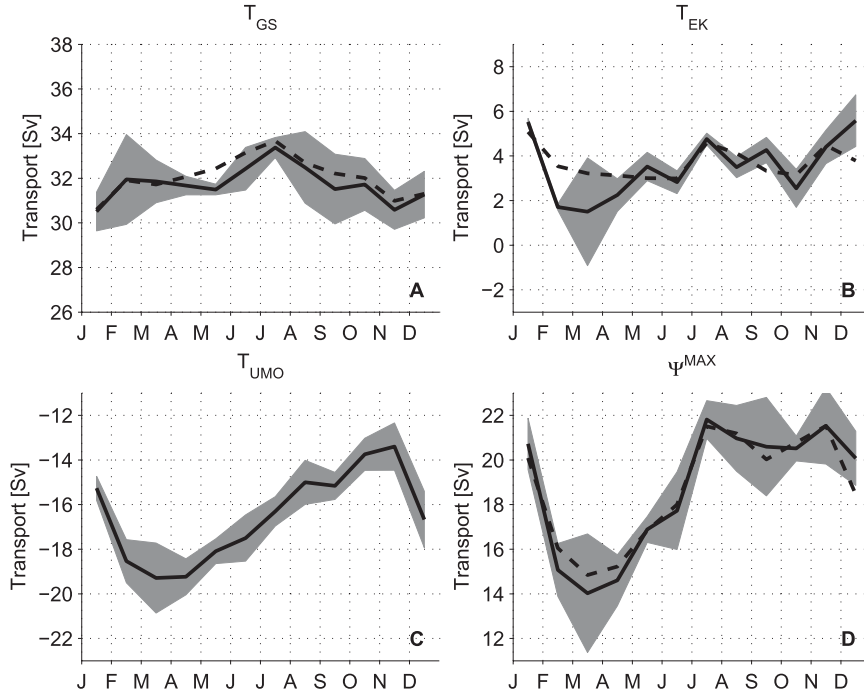


FIG. 10. Seasonal cycles (black solid lines) of (a) T_{GS} , (b) T_{EK} , (c) T_{Umo} , and (d) Ψ^{MAX} , as obtained from month-wise averages of the time series between April 2004 and April 2008. The gray envelopes represent the standard error of each month (as obtained from the four realizations of monthly averages that are available for each month). The dashed lines in (a) and (b) represent seasonal cycles of T_{GS} and T_{EK} based on the 26-yr-long time series (October 1982–January 2008) used for the computation of the spectra in Fig. 8. The dashed line in (d) represents the best guess of the long-term seasonal cycle of Ψ^{MAX} (see text). Positive values denote northward flow.

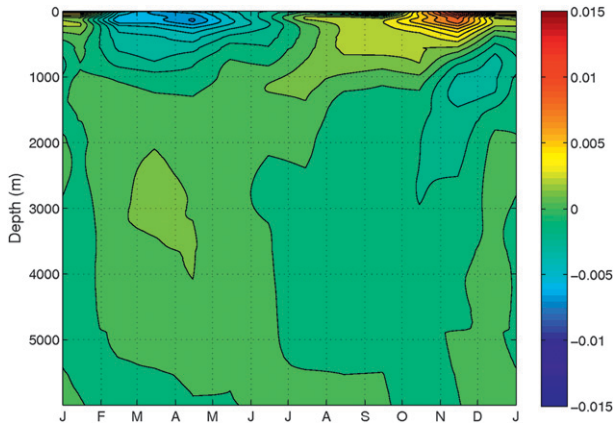


FIG. 11. Monthly-mean midocean transport profile (Sv m^{-1}) for the period April 2004–08, after removal of the annual mean and the barotropic (vertical mean) flow for each month.

The seasonal wind stress curl anomaly along 26.5°N (Fig. 13a) has a semiannual cycle over most of the basin. The largest signal, however, occurs at the eastern boundary, which is annual in nature with a pronounced anticyclonic curl anomaly in summer and cyclonic anomaly in winter (Figs. 13a,b). It is caused by strong summertime intensification of northerly winds adjacent to the eastern boundary and their relaxation in winter.

Figure 14a shows the resulting model-predicted variation of the midocean transport profile across the basin, $T_{\text{MO}}^{\nabla \times \tau}(z)$ —computed according to (8)–(10)—where we have summed the response of the first two baroclinic modes, with $H_{\text{mix}} = 100 \text{ m}$ (higher baroclinic modes have a negligible contribution). There is a good correspondence between the observed interior $T_{\text{MO}}(z)$ seasonal cycle and the model prediction (Fig. 10). The seasonal AMOC anomaly associated with the model-predicted midocean transport $T_{\text{UMO}}^{\nabla \times \tau}$ (calculated as the upper-ocean

transport anomaly) is approximately 4.3 Sv peak to peak (Fig. 14b, blue line), and its amplitude and phase are comparable to that of the observed T_{UMO} seasonal cycle (5.9 Sv) of Fig. 10c. The model suggests that this response is due almost entirely to internal pressure variations at the eastern boundary (Fig. 14b, green line), which in turn are due to the dominance of the wind stress curl signal at the eastern boundary (Figs. 13a,b). There is good agreement between the model's eastern boundary seasonal transport cycle of 4.2 Sv peak to peak and the observed eastern boundary contribution $\Psi_{\text{MOE}}^{\text{MAX}}$ (Fig. 12b) in both amplitude (5.4 Sv) and phase [maximum (minimum) northward transport in October (April)]. Essentially, the model implies that the seasonal variation of the zonally integrated interior flow profile is almost entirely attributable to changes in stratification at the eastern boundary, caused by local wind stress curl variations that uplift (depress) density surfaces in the spring (fall), which follow, in quadrature, the winter (summer) periods of enhanced cyclonic (anticyclonic) curl at the eastern boundary.

While largely consistent with the basinwide integrated flow, the simple linear wave model has many limitations. It only allows for purely zonal propagation of northward transport anomalies. It also does not include the effect of horizontal mean flow (and vertical shear) on the anomalies or the impact of topography, as anomalies generated on the eastern boundary move westward (e.g., Killworth and Blundell 2005). It therefore cannot be expected to give an accurate description of the zonal distribution of northward flows in the basin interior along 26.5°N .

The midocean variability predicted by the model is distinct from the quasi-stationary topographic Sverdrup response of the ocean interior to the wind stress curl forcing, which depends on the zonally integrated wind

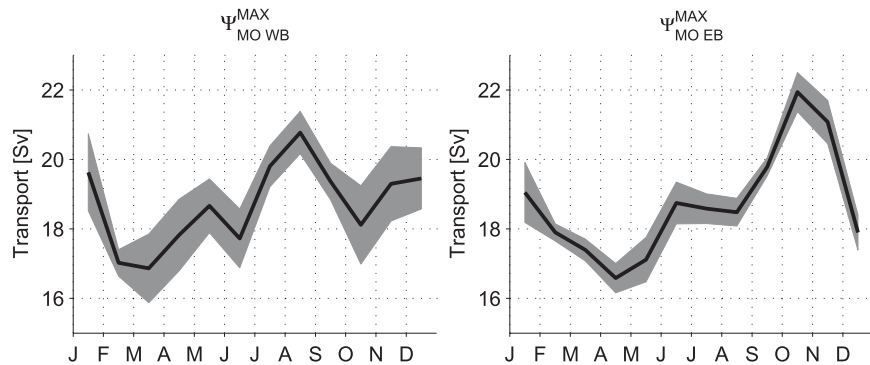


FIG. 12. Seasonal cycles of the (left) western and (right) eastern boundary contributions to the midocean section of the overturning strength ($\Psi_{\text{MOW}}^{\text{MAX}}, \Psi_{\text{MOE}}^{\text{MAX}}$) based on the time series shown in Fig. 9. The gray envelope represents the standard error as in Fig. 10. Positive values correspond to northward flow. The sum of the seasonal anomalies of $\Psi_{\text{MOW}}^{\text{MAX}}$ and $\Psi_{\text{MOE}}^{\text{MAX}}$ therefore corresponds to the seasonal anomalies of T_{UMO} .

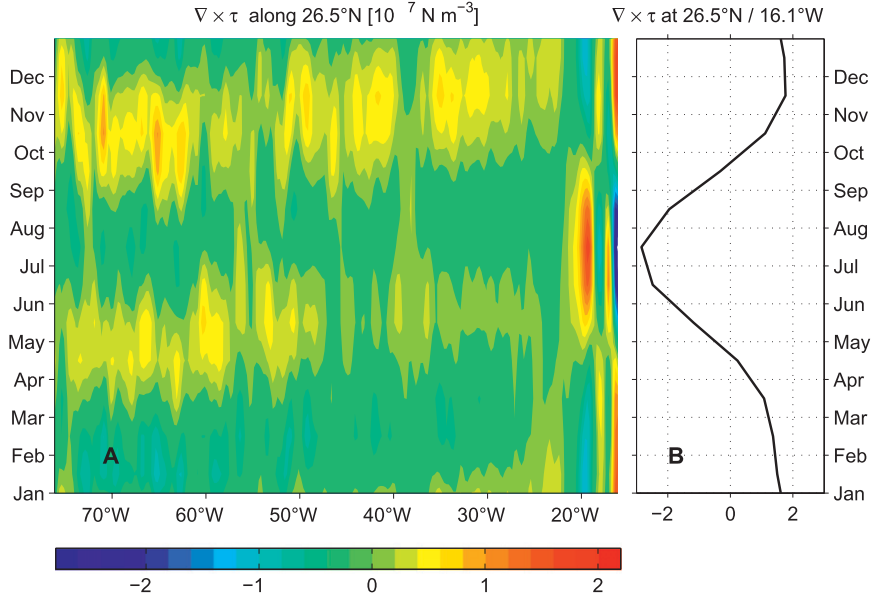


FIG. 13. (a) Seasonal wind stress curl anomaly (10^7 N m^{-3}) along 26.5°N relative to annual mean value based on SCOW climatology (Risien and Chelton 2008). This field is used to force the midocean response analysis illustrated in Fig. 14. (b) Wind stress curl anomaly extracted at $26.5^\circ\text{N}, 16.1^\circ\text{W}$ from the data shown in (a). The wind stress curl variability is largest near the eastern boundary, where strong seasonal variations in southward winds along the African coast (maximum in boreal summer) produce a large seasonal cycle.

stress curl across the entire basin. It is well established from theory and models (Anderson and Gill 1975; Anderson and Corry 1985) and observations (Lee et al. 1996) that, on seasonal time scales, this response is carried primarily in the barotropic mode. This circulation is essentially transparent to our array and has no effect on Ψ^{MAX} . The *baroclinic* response of the interior depends on the density differences between the eastern and western boundaries, which instead are related to first order to the *differences* in wind stress curl forcing at the eastern and western boundaries, which are the fundamental dynamics expressed in the above model.

5. Discussion

a. Seasonal cycle

From a global perspective, the seasonal anomalies of Ψ^{MAX} are thought to be dominated by fluctuations of the Ekman transport, compensated for by a nearly depth-independent geostrophic return flow below the Ekman layer (Jayne and Marotzke 2001; Böning et al. 2001; Wunsch and Heimbach 2009). Jayne and Marotzke point out that the seasonal cycle of the northward Ekman transport and of the meridional overturning circulation are on average symmetric about the equator with nodes at the equator and 20°N/S . We have shown that T_{GS} and T_{UMO} exceed T_{EK} in terms of both amplitude of the

seasonal cycle and rms fluctuations on seasonal time scales. The mostly geostrophic seasonal cycle of T_{UMO} of 5.9 Sv peak to peak at 26.5°N is comparable in amplitude with the maximum seasonal cycles of T_{EK} in the North Atlantic, which are found in the tropics (10 Sv) and at midlatitudes (6 Sv). One might therefore speculate that throughout the Atlantic the contribution of geostrophic upper-ocean transports to seasonal anomalies of Ψ^{MAX} might be comparable to that of T_{EK} (Hirschi et al. 2007). This is consistent with repeated hydrographic observations at 35°S in the Atlantic (Baringer and Garzoli 2007; Garzoli and Baringer 2007).

Our measurements suggest that the largest part of the seasonal cycle of T_{UMO} is driven by density anomalies at the eastern boundary of the Atlantic. Chidichimo et al. (2010) find coherent seasonal anomalies in density in the depth range between 100 and 1400 m at the mooring sites on the upper continental slope of the eastern boundary, while 1000 km offshore no significant seasonal density anomalies are found at depths in excess of 100 m. It is therefore plausible that the transport anomalies that dominate the seasonal cycle of T_{UMO} do not correspond to basin-scale coherent flows but, rather, are concentrated in a narrow band along the eastern boundary. This concept is consistent with the observed near-eastern-boundary intensification of the seasonal wind stress curl anomalies.

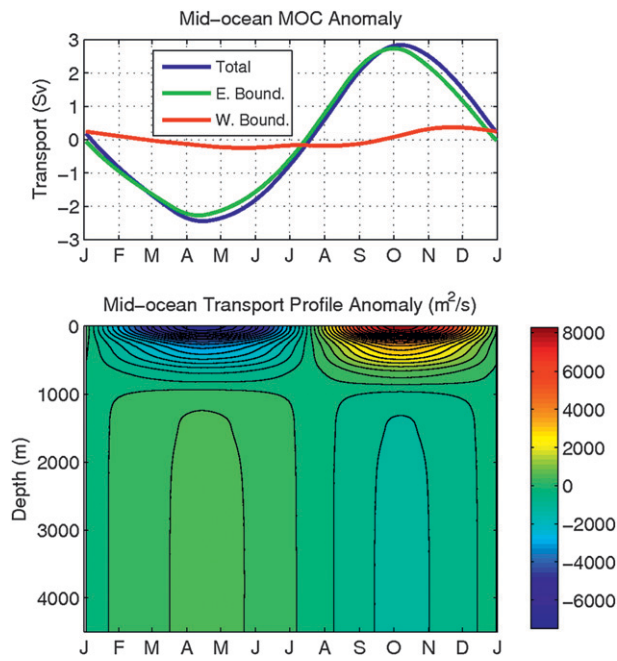


FIG. 14. The midocean response from the forced Rossby wave model [Eqs. (8)–(10)], using the SCOW seasonal wind stress curl anomaly climatology (Fig. 13), summed over the first two baroclinic modes. (a) The resulting anomaly of $T_{MO}^{V \times \tau}(z)$. (b) The associated anomaly Ψ_{MO}^{MAX} calculated as the transport anomaly in the upper-ocean above the zero level (~ 950 m) of the $T_{MO}^{V \times \tau}(z)$. The curves in (b) show the total AMOC anomaly (blue), and the contributions resulting from the variability forced at the eastern boundary (green) and at the western boundary (red).

b. Wind stress curl forcing of seasonal anomalies of Ψ^{MAX}

The response of T_{UMO} to the seasonal cycle in wind stress curl along 26.5°N has been simulated in a linear “Rossby wave model,” which implies that the seasonal variation of T_{UMO} is almost entirely attributable to changes in stratification at the eastern boundary, caused by local wind stress curl variations. Orography, sea surface temperature gradients, and ocean currents are known to affect wind stress curl (Chelton et al. 2004) as (i) constrictions due to sloping continental orography, island tips, and interisland gaps create jet winds and (ii) differential heating of the marine atmospheric boundary layer across an SST front accelerates wind over warm waters and decelerates it over cold waters. In the annual mean fields there is a narrow band of coherent positive wind stress curl along the eastern margin of the Atlantic from south of Cape Vert near 15°N to Cape Finisterre near 43°N (Fig. 2 of Chelton et al. 2004).

Ongoing studies based on QuikSCAT data suggest that seasonal anomalies in wind stress curl in the tropical/subtropical Atlantic are meridionally coherent (1000-km scale) along the eastern boundary (not shown), but with

rather small zonal scales, and may be related to a seasonal pattern with alternating signs in the zonal direction extending westward from the coast to about 19.5°W , resulting from orographic jet winds induced by the Canary islands and Cape Yubi (at 28°N on the Moroccan coast). Hence, we expect the seasonality in T_{UMO} at 26.5°N to have a large meridional coherence scale, modulated locally by jet winds. It has been demonstrated that orography, SST gradient, and ocean current effects on the wind stress curl along continental margins are poorly represented in datasets, such as the National Centers for Environmental Prediction–National Center for Atmospheric Research reanalysis (Chelton et al. 2004), that are routinely used to drive ocean models. Yet our Rossby wave model suggests that these effects may drive the seasonal cycle in the circulation. Kanzow et al. (2009) showed that an eddy-resolving ($1/12^{\circ}$) numerical model significantly underestimated the variability of T_{UMO} at 26.5°N owing to unrealistically small density fluctuations at the ocean margins. If this is a general problem of even high-resolution, eddy-resolving numerical models, the true impact of *upper-ocean geostrophic transports* (i.e., the sum of T_{UMO} and T_{GS}) on intraseasonal to seasonal variations of Ψ^{MAX} may be much larger than model simulations imply. Fennel and Lass (2007) argue that realistic wind stresscurls along ocean margins are required to realistically simulate the vertical structure of the near-coastal thermocline and currents in ocean models. The mechanism of near-boundary seasonal wind stress curl anomalies affecting T_{UMO} via local uplift/depression of isopycnals (Köhl 2005; Chidichimo et al. 2010) is reminiscent of a mechanism of multiannual variability of T_{UMO} in the subtropical North Atlantic as recently proposed by Cabanes et al. (2008).

c. Is the variability in Ψ^{MAX} observed between April 2004 and April 2008 representative of longer periods?

There is not, nor has there been, any other AMOC observing system in place for comparing our results. Therefore, the long-term representativeness (particularly of T_{UMO}) can only be assessed indirectly. A large body of literature exists on hydrographic variability on intra-seasonal to decadal periods in the North Atlantic (e.g., Roemmich and Wunsch 1985; Joyce and Robbins 1996; Joyce et al. 1999; Johnson and Gruber 2007; Cunningham and Alderson 2007; Kieke et al. 2009). However, there is no straightforward link between changes in hydrographic properties and changes in Ψ^{MAX} . For example, the strength of the AMOC-related Labrador Sea outflow along the western boundary appears to have been stable despite a decade-long warming trend in the outflow waters (e.g., Schott et al. 2006). A further complication for

the interpretation of historical hydrographic data in terms of Ψ^{MAX} is that density measurements away from the ocean boundaries (even few tens of kilometers away) do not provide a strong constraint on AMOC transport variability at 26.5°N (Kanzow et al. 2009) because of eddy noise.

Unfortunately, a similar limitation applies to satellite altimetry data that otherwise could be considered as a promising way to extend our time series back in time. Kanzow et al. (2009) have shown that sea surface height (SSH) differences between the eastern and western boundary cannot be used to infer the temporal variability of T_{UMO} at 26.5°N. They argue that this is primarily due to the more complex vertical structure of the flow close to the ocean boundaries, which inhibits a simple projection of SSH on the first baroclinic mode (in contrast to the offshore ocean). The results are in agreement with simulations based on a numerical model by Hirschi et al. (2009).

Currently, simulations from numerical models are probably the only source for long, daily AMOC time series exceeding our 4-yr measurement period. In their ocean state estimate Wunsch and Heimbach (2009) find a dominant seasonal tropical Ekman transport response, which is in line with the results of Jayne and Marotzke (2001). Whether the state estimate successfully captures the observed seasonal anomaly in T_{UMO} at 26.5°N is unclear. In general, the degree of realism of fluctuations in T_{UMO} in assimilation products will depend (among other things) on purposeful observations that provide strong constraints on the basinwide integrated northward flow. Hydrographic measurements away from the ocean boundaries or SSH do not fall in this category (Kanzow et al. 2009). This view is supported by the findings of Smith et al. (2009), who show that the assimilation of hydrographic data from Argo floats into a numerical model fails to improve the temporal variability of Ψ^{MAX} , when compared with the RAPID–MOC/MOCHA time series. They conclude that density measurements across the ocean margins are required to constrain the flow. The scarcity of such observations might also explain why today's state-of-the-art ocean state estimates (even when carefully constrained by the same observations) remarkably differ from one another in terms of the strength and temporal variability of Ψ^{MAX} (Lee 2009).

In this study wind stress curl at the eastern boundary has been identified as a possible driving mechanism of the seasonal cycle of T_{UMO} . Assuming that this relationship is robust, the representativeness of the seasonal cycle in T_{UMO} (derived from the 4-yr measurement period) of longer measurement intervals will be linked to the representativeness of the seasonal cycle of the wind stress curl. The QuikSCAT high-resolution wind measurements

started in 1999. From daily gridded wind stress data (horizontal resolution of $0.25^\circ \times 0.25^\circ$), the monthly mean wind stress curl was computed close to upper-ocean density moorings (EBH4, EBH5). Figure 15 reveals that the seasonal cycle is a rather regular feature at the eastern boundary over the 12-yr interval, in both phase and amplitude. It clearly dominates the variability at this location, as each of the January values in the 1999–2009 interval is larger than each of the July ones. In addition, the seasonal cycle in wind stress curl from the 2004–08 interval (bold dashed line) is almost identical to that from the 1999–2009 interval (bold solid line). The observed seasonal cycle of T_{UMO} may therefore be representative of the last decade and even longer periods.

If the seasonal cycle of T_{UMO} is a long-term persistent feature of the ocean circulation at 26.5°N, it is likely that the inference of decadal trends in Ψ^{MAX} based on hydrographic snapshots might suffer from seasonal biases. Bryden et al. (2005b) deduced a decline in Ψ^{MAX} of 8 Sv between 1957 and 2004 using the five hydrographic sections shown in Fig. 16 (filled squares and Table 2). They used constant values for T_{EK} and T_{GS} , leaving T_{UMO} as the only time-variable component of Ψ^{MAX} . Based on our analysis, the months of the first and last cruises (October and April) correspond to the maximum and minimum in the seasonal cycle of T_{UMO} (Fig. 10c) such that the 1957 and 2004 estimates are likely to be biased high and low, respectively. If we subtract the seasonal anomalies of T_{UMO} (shown in Fig. 10c) from the hydrographic estimates, by taking into account the months in which the cruises were conducted (Table 2), the resulting “de-seasoned” time series of Ψ^{MAX} (open diamonds, Fig. 16) exhibits a reduction in variance of more than 80% and does not show a persistent decline. The efficiency of the seasonal bias correction in removing variance implies that aliasing due to seasonal anomalies possibly accounts for a large part of the trend found by Bryden et al. (2005b).

d. What are the meridional scales associated with the seasonal anomalies?

In the climate context, it would be instructive to know what the meridional scales of the seasonal anomalies in Ψ^{MAX} (and of the associated meridional heat transport) are. Are the seasonal anomalies a local phenomenon [i.e., associated with an eddy decorrelation scale of $O(100 \text{ km})$ or less] or is their meridional extent of $O(1000 \text{ km})$? To answer this question, simultaneous continuous measurements of density along the ocean margins at different latitudes and depth levels would be required. As mentioned above, such observations are very rare, and this represents a major gap in today's ocean observing system.

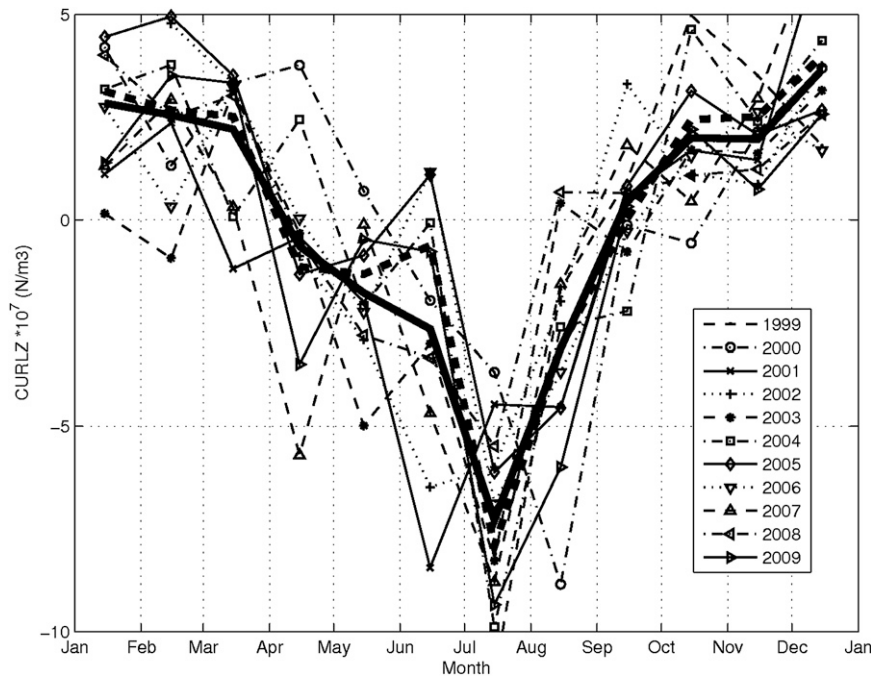


FIG. 15. Monthly anomalies of the wind stress curl (10^7 N m^{-3}) at 27.25°N , 14.50°W near the eastern boundary density moorings EBH4 and EBH5. Each thin line represents one year of monthly averaged data between 1999 and 2009. The bold lines represent seasonal cycles [2004–08 average (dashed) and 1999–2009 average (solid)]. Data source is the $0.25^\circ \times 0.25^\circ$ gridded QuikSCAT scatterometer wind stress from the Jet Propulsion Laboratory (available online at http://podaac.jpl.nasa.gov/DATA_CATALOG/quikscatinfo.html).

A handle on the meridional scales of anomalies in $T_{U\text{MO}}$ (or Ψ^{MAX}) may indirectly be obtained from numerical models and/or plausibility arguments. Kanzow et al. (2009) concluded from a combination of RAPID–MOC/MOCHA observations, altimetry, and a high-resolution numerical model that the impact of local eddies on $T_{U\text{MO}}$ at 26.5°N was rather small. Numerical model results from Hirschi et al. (2007), relying on monthly values, suggest that anomalies of the *thermal wind* component of Ψ^{MAX} (i.e., the Ekman and external component subtracted) at 26.5° display a meridional decorrelation scales of roughly 1000 km.

Numerical models have shown that Ψ^{MAX} at low latitudes in the Atlantic (including 26.5°N) is highly correlated with the advective meridional heat transport (e.g., Böning et al. 2001; Kanzow et al. 2008b), and this has been confirmed from an analysis of the RAPID–MOC/MOCHA measurements (Johns et al. 2010, manuscript submitted to *J. Climate*). Further, it has been shown that the meridional divergence of advective meridional heat transport nearly balances upper-ocean heat storage on seasonal time scales at low latitudes, whereas toward higher latitudes, air-sea heat fluxes are of primary importance (e.g., Jayne and Marotzke 2001). This study suggests that seasonal geostrophic upper-ocean transport fluctuations

are stronger than previously thought. Therefore, the possible meridional divergence of these fluctuations might represent an important contribution to low-latitude, seasonal heat storage anomalies.

Johns et al. (2010, manuscript submitted to *J. Climate*) find that a change in Ψ^{MAX} of 1 Sv at 26.5°N corresponds to a change in advective heat transport of $0.06 \times 10^{15} \text{ W}$. A simple calculation shows that meridional divergence in upper-ocean geostrophic flow of 2 Sv between two transatlantic sections separated by 1000 km over the course of 6 months would lead to a net temperature change of 0.2°C in the upper 500 m (if there is no exchange with the atmosphere). Since heat storage will not be spatially uniform, local changes (near the ocean margins) larger than this on seasonal periods are likely. In contrast anomalous $T_{U\text{MO}}$ associated with an eddy scale of $O(100 \text{ km})$ would correspond to a 2°C anomaly, which is far more than we observe at the various measurement sites. From these considerations we assume that the meridional extent of the seasonal anomalies is likely to be $O(1000 \text{ km})$ rather than being set by localized eddy processes.

Possible seasonal storage of heat by large-scale divergences of geostrophic upper-ocean transport may be important for regional oceanic and of near-boundary continental climates, if the heat is (partly) released to the

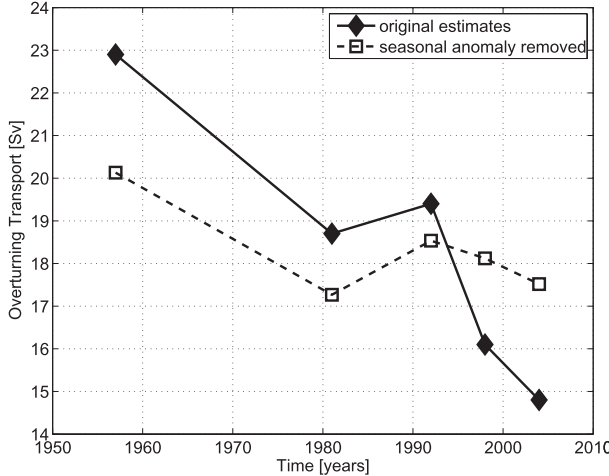


FIG. 16. The Ψ^{MAX} inferred from five hydrographic snapshot estimates between 1957 and 2004 (solid diamonds), as reproduced from Bryden et al. (2005b). The hydrography cruises were carried out in different seasons, namely, in October 1957, August–September 1981, July–August 1991, February 1998, and April 2004. The open squares represent the historical estimates of Ψ^{MAX} with seasonal anomalies of T_{UMO} (Fig. 10c; Table 2) subtracted.

atmosphere. Near-surface seasonal heat storage at low latitudes may represent a nonnegligible source of energy for tropical cyclones. However, given that wind stress curl forcing along coastal margins may be unrealistically small in OGCMs, simultaneous, continuous observations of upper-ocean geostrophic transport across two or more zonal transects would be needed to observe the possible existence of strong upper-ocean meridional geostrophic transport divergence.

6. Conclusions

- Between April 2004 and April 2008, the strength of the AMOC, Ψ^{MAX} , at 26.5°N has a mean of 18.7 ± 2.1 Sv and rms fluctuations of 4.8 Sv. At periods shorter than 100 days, T_{EK} variability dominates over T_{GS} and T_{UMO} , while at seasonal time scales Ψ^{MAX} variability is dominated by T_{UMO} and T_{GS} .
- The total western boundary contribution Ψ_W^{MAX} (i.e., T_{GS} plus the western boundary contribution of the upper-midocean component $\Psi_{\text{MOW}}^{\text{MAX}}$) to “seasonal variability” (180-day low passed) is significantly larger than that of the eastern boundary $\Psi_{\text{MOE}}^{\text{MAX}}$ (2.0 Sv versus 1.3 Sv rms).
- The best estimate of the long-term peak-to-peak amplitude of the seasonal cycle of Ψ^{MAX} is 6.7 Sv. From the three transport components T_{UMO} has the most pronounced seasonal cycle of 5.9 Sv peak to peak with a maximum northward upper-ocean transport in autumn and a minimum in spring. The T_{UMO} cycle is

TABLE 2. Seasonal bias correction of the Bryden et al. (2005b) historical estimates of Ψ^{MAX} (see Fig. 16). Corrections have only been applied to the upper-midocean transport (T_{UMO}), as Bryden et al. used constant values for T_{EK} and T_{GS} (see text). Columns 1–4 give the cruise dates, the historical estimates of Ψ^{MAX} (solid line in Fig. 16, Bryden et al.), the seasonal anomalies of T_{UMO} (from Fig. 10c) corresponding to the months in which the measurements cruises were conducted, and the seasonal-anomaly-corrected estimates of Ψ^{MAX} (dashed line in Fig. 16), respectively.

Cruise	Ψ^{MAX} with		
	Ψ^{MAX} (Sv)	T_{UMO} seasonal anomaly (Sv)	seasonal anomaly removed (Sv)
Oct 1957	22.9	2.8	20.1
Aug–Sep 1981	18.7	1.4	17.3
Jul–Aug 1992	19.4	0.9	18.5
Feb 1998	16.1	-2.0	18.1
Apr 2004	14.8	-2.7	17.5

dominated by the density contribution from the eastern boundary, which has a peak-to-peak amplitude of 5.4 Sv.

- The response of T_{UMO} to the seasonal cycle in wind stress curl along 26.5°N has been simulated in a linear “Rossby wave model.” The modeled and observed seasonal cycle of T_{UMO} agree both in phase and amplitude. The model implies that the seasonal variation of T_{UMO} is almost entirely attributable to changes in stratification at the eastern boundary, caused by local wind stress curl variations that uplift (depress) density surfaces in the spring (fall) that follow, in quadrature, the winter (summer) periods of enhanced cyclonic (anticyclonic) curl at the eastern boundary.

Acknowledgments. The authors thank the captains and crews of the R/Vs *Charles Darwin*, *Discovery*, *Ronald H. Brown*, *Knorr*, *Poseidon*, and *Seward Johnson*; and the UKORS, RSMAS, and AOML mooring and hydrography teams. The mooring operations have been supported by the Natural Environment Research Council (NERC) RAPID program, the U.S. National Science Foundation (NSF) under Grant 0728108, and the U.S. National Oceanic and Atmospheric Administration Western Boundary Time Series program. The Florida Current cable data are made freely available by the Atlantic Oceanographic and Meteorological Laboratory (available online at www.aoml.noaa.gov/phod/floridacurrent/) and are funded by the NOAA Office of Climate Observation. The wind stress data were obtained from CERSAT at IFREMER, Plouzané (France). We thank Darren Rayner (NOCS) for coordinating the U.K. seagoing activities and for leading the mooring data recovery. Two of the authors (TK and JJMH) were supported in the framework of the NERC-funded Rapid Climate Change Program (Grant 880

NER/T/S/2002/00481). We thank the two anonymous reviewers for their detailed criticism, which led to significant improvement of the manuscript.

APPENDIX A

Computation of Internal Transport T_{INT}

In the following we describe how the northward geostrophic internal transport T_{INT} [which is required to estimate T_{MO} in (5)] is computed. This study differs from the approach taken by Cunningham et al. (2007) and Kanzow et al. (2007) in two ways. First, density measurements from both eastern and western flanks of the MAR (Fig. 2) are included in the calculations to account for potential pressure gradients across it, as the AABW piles up against the western flank of the MAR. Mooring MAR1 (on the western MAR flank) gives a density profile over the whole water column, whereas MAR2 (on the eastern flank) covers the 2500–5000-m range. Accordingly, we can split $T_{\text{INT}}(z)$ into a western ($T_{\text{INT_W}}$) and eastern ($T_{\text{INT_E}}$) basin contribution. In the upper 4740 m of the water column, $T_{\text{INT_W}}$ is computed from the density difference between MAR1 and WB2 (relative to −4740 m) according to

$$T_{\text{INT_W}}(z) = -g/(f\rho) \int_{Z_{\text{REF}}}^0 [\rho_{\text{MAR1}}(z') - \rho_W(z')] dz \quad (\text{A1})$$

for $z < 4740$ m. Second, we account for the net northward transport in the AABW layer (McCartney and Curry 1993; Bryden et al. 2005b) that is not part of the measurement campaign. This way, comparisons of the magnitude of Ψ^{MAX} between hydrography-derived estimates including the AABW range (Bryden et al. 2005b) and this study are free from potential biases resulting from different vertical ranges of the underlying transport profiles. The $T_{\text{INT_W}}(z, t)$ is extended in the vertical to 6000 m with a time-invariant AABW transport-per-unit-depth profile $T_{\text{AABW}}(z)$, as shown in Fig. A1. The latter represents a smoothed approximation of five historical transport profiles across 26.5°N, estimated from hydrographic measurements (Bryden et al. 2005b). Here $T_{\text{AABW}}(z)$ spans the 5000–6000-m depth range. An offset c is added to the $T_{\text{AABW}}(z)$ profile such that finally a time-mean northward transport of $T_{\text{AMOC}}(z)$ of 2.1 Sv at depths exceeding 5000 m is obtained, representing the average of the five estimates from Bryden et al. (2005b),

$$T_{\text{INT_W}}(z, t) = T_{\text{AABW}}(z) + c, \quad (\text{A2})$$

for $5000 \text{ m} < z < 6000 \text{ m}$. The gap between 4740 and 5000 m is filled by vertical interpolation (using a cubic spline) between the time mean of $T_{\text{INT_W}}(z)$ above 4740 and below 5000 m, ensuring a smooth transition. Hence, for $z > 4740 \text{ m}$ $T_{\text{INT_W}}(z)$ is time invariant.

At 26.5°N the MAR crest height is at about 2500 m. Major deep trenches, such as the Romanche (equator), Vema (11°N), and Kane (24°N) Fracture Zones, cut through the MAR and thus allow for a zonal exchange of deep and bottom waters in excess of 3700 m (Mercier and Speer 1998). At depths greater than the intermediate water level, isotherms along 26.5°N spread almost horizontally across the basin up to a depth of 3700 m. Below that northward transport of AABW manifests itself in an upward slope of western basin isotherms toward the MAR. Consequently, we assume that the MAR is permeable at depths shallower than 3700 m. Based on this, $T_{\text{INT_E}}(z, t)$ is computed as follows. In the 3700–4740-m range transports are computed from the density difference between the eastern boundary and MAR2 (relative to 4740 m):

$$T_{\text{INT_E}}(z) = -g/(f\rho) \int_{-4740}^{-3700} [\rho_E(z') - \rho_{\text{MAR2}}(z')] dz \quad (\text{A3})$$

for $-4740 \text{ m} < z \leq -3700 \text{ m}$. Shallower than 3700 m $T_{\text{INT_E}}(z, t)$ is obtained from the eastern boundary to MAR1 density difference relative to the time-variable value of $T_{\text{INT_E}}(z = -3700 \text{ m})$ as derived from (A3):

$$T_{\text{INT_E}}(z) = -g/(f\rho) \int_{-3700}^0 [\rho_E(z') - \rho_{\text{MAR1}}(z')] dz + T_{\text{INT_E}}(-3700) \quad (\text{A4})$$

for $z \geq 3700 \text{ m}$. We assume there is no vertical shear in $T_{\text{INT_E}}(z, t)$ below 4740 m according to

$$T_{\text{INT_E}}(z, t) = 0 \quad \text{for } z < -4740 \text{ m}. \quad (\text{A5})$$

Here $T_{\text{INT}}(z)$ integrated between the western boundary (WB2) and the eastern boundary is then given by the sum of the eastern and western contributions according to

$$T_{\text{INT}}(z) = T_{\text{INT_W}}(z) + T_{\text{INT_E}}(z). \quad (\text{A6})$$

APPENDIX B

Error Bars

Uncertainties in time-mean transports can come from three sources: (i) measurement errors (temperature,

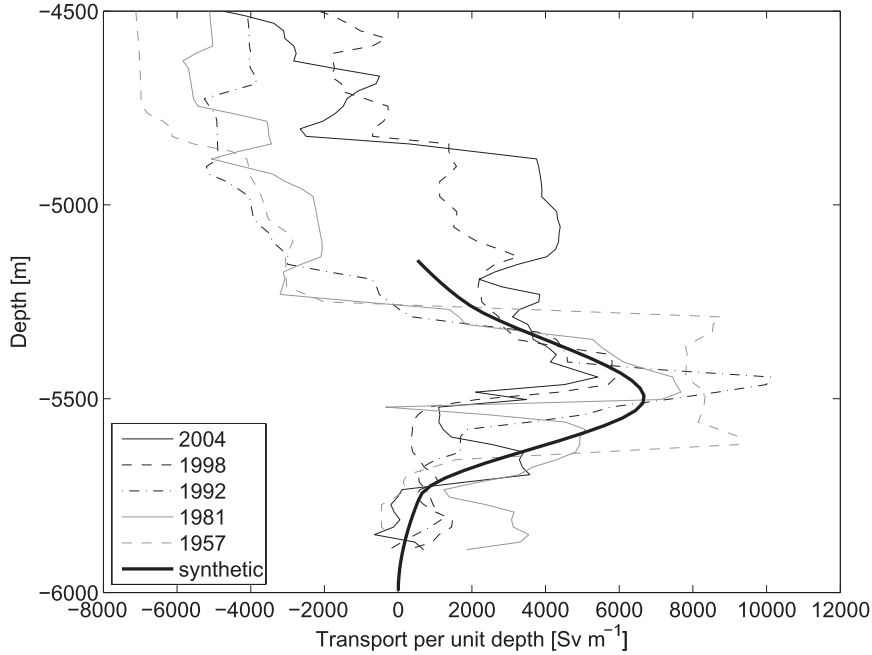


FIG. A1. Abyssal, zonally integrated transport across 26.5°N from hydrographic cruises in 1957, 1981, 1992, 1998, and 2004 (as presented by Bryden et al. 2005b). The synthetic approximation of the transports below 5000 m (bold black line) represents the transport shear profile used in this study to extend the AMOC transport profile $T_{\text{AMOC}}(z)$ into the AABW range.

conductivity, velocity, wind stress, cable voltage), (ii) model errors (e.g., geostrophic approximation; compensation), and (iii) the time variability of the transport signal (standard errors). The measurement errors consist of two parts: random errors and possible bias errors. A detailed error analysis for a precursor experiment near 26.5°N (Johns et al. 2005; Kanzow et al. 2006) has an error in baroclinic transports (i.e., T_{INT}) of 2.5 Sv rms. The precursor experiment used a lower number of vertical density sampling levels, less precise temperature sensors, and very few pressure measurements and no conductivity measurements. On the basis of this, we estimate the error in instantaneous (i.e., 10-day low-pass filtered) measurements of top-to-bottom integrated $T_{\text{INT}}(z)$ is less than 2.0 Sv rms. The contribution of the instantaneous uncertainty in T_{INT} to that of Ψ^{MAX} will be less than 1.5 Sv rms as a result of the application mass compensation (reduction of 25%). The errors in T_{INT} arise from both uncertainties in the T , C , and P sensors and vertical interpolation between the discrete measurement levels. As the sensors are replaced and carefully calibrated each year, potential biases in the 4-yr average sensor-related uncertainties are expected to be small. The interpolation-related uncertainty is mostly random, even if the sampling levels do not change over time [see Fig. 18 of Johns et al. (2005)]. Therefore, the uncertainty of the 4-yr mean will be substantially smaller than the instantaneous

uncertainty. We therefore expect the remaining 4-yr-mean bias of Ψ^{MAX} (and $T_{U\text{MO}}$) resulting from uncertainties in T_{INT} to be not larger than ± 1.0 Sv.

Errors in daily mean instantaneous (3-day low-pass filtered) measurements of T_{GS} amount to 1.7 Sv rms with the errors being mostly random (Larsen 1992; Meinen et al. 2010). Here T_{GS} is regularly corrected for potential biases using independent estimates of T_{GS} from calibration cruises (relying on velocity measurements from dropsondes). A conservative estimate of the 4-yr-averaged uncertainty in T_{GS} is ± 0.5 Sv. This is based on the fact that six or more cable calibration cruises per year are performed on average, yielding more than 24 independent calibration points over the 4-yr record, each with ± 1.7 -Sv accuracy, and therefore a mean transport bias of $1.7/\sqrt{24} = 0.3$ Sv. We estimate the possible 4-yr mean bias in T_{EK} is ± 0.5 Sv (resulting from uncertainties in both wind measurements and the drag coefficient). We consider this estimate to be rather conservative as (i) it amounts to 15% of the observed time mean of T_{EK} and (ii) rms differences in T_{EK} between instantaneous values from QuikSCAT and the NCEP-NCAR reanalysis amount to 0.5 Sv rms. The instantaneous error in T_{WBW} yields 0.4 Sv rms (including possible mean biases), based on comparisons between lowered acoustic Doppler and the moored current measurements at the western boundary for T_{WBW} . The 4-yr-mean bias of T_{WBW} should be of $O(\pm 0.2$ Sv).

Instantaneous measurements of T_{AABW} do not exist, and so the uncertainty of both instantaneous and time-mean values is difficult to estimate. The standard deviation of the five snapshot estimates of AABW transport at 26°N (Bryden et al. 2005b) is 0.5 Sv. The true uncertainty instantaneous measurements of T_{AABW} might be somewhat larger because of possible undersampling of the deep transport signal over rough bathymetry (Ganachaud 2003a), say, less than 1.0 Sv rms. The effect of a 1.0-Sv uncertainty in T_{AABW} to that in Ψ^{MAX} is less than 0.2 Sv rms. This is because compensation transport $T_C(z)$ (see [4]) is essentially barotropic, so that the compensation for the error contribution of T_{AABW} is distributed almost uniformly in the vertical. As Ψ^{MAX} is an integral over approximately the upper 1000 m and the average depth of the section is around 5000 m, the errors contributing to Ψ^{MAX} amount to only about 20% of the uncertainty in T_{AABW} . Therefore the 4-yr-average bias in Ψ^{MAX} from this contribution should be less than 0.2 Sv. If there is a mean 1-Sv net transport across 26.5°N resulting from the inflow into the Arctic through the Bering Strait, this can only show up in our array as a barotropic component (since all vertically sheared flow is accounted for in T_{INT}). If one added this to the observed (mass balanced) profile, and integrated from the surface downward to h_{ZC} , it would add an uncertainty to Ψ^{MAX} of about 0.2 Sv (or 20% of 1 Sv).

Combining the above error estimates as root-sum-square, we estimate the measurement error for the 4-yr average of Ψ^{MAX} is ± 1.3 Sv (from rms errors of T_{INT} 1.0 Sv, T_{GS} 0.5 Sv, T_{EK} 0.5 Sv, T_{WBW} 0.2 Sv, T_{AABW} 0.2 Sv, and the Bering Strait imbalance 0.2 Sv).

It is beyond the scope of this paper to discuss the model-related errors. Scaling arguments imply that the errors in using the geostrophic and Ekman approximations for our application are on the order of 3% (Kanzow 2000). The standard error of a time series can be estimated as the standard deviation divided by the square root equivalent degrees of freedom (DOF). To estimate the DOF, we divide the time series length by the integral time scale. We define the integral time scale as the sum of the autocorrelation from minus zero crossing to plus zero crossing (Tennekes and Lumley 1972). The results are summarized in Table 1. The division of the observational period of 1450 days by the integral time scale then gives the DOF. The standard errors of Ψ^{MAX} , T_{GS} , T_{EK} , and T_{UMO} amount to 0.8, 0.4, 0.3, and 0.6 Sv, respectively.

Therefore the total uncertainty of the 4-yr mean Ψ^{MAX} (representing the sum of the measurement error and standard errors) amounts to $1.3 \text{ Sv} + 0.8 \text{ Sv} = 2.1 \text{ Sv}$. In principle the two errors could also be combined randomly, since they have arbitrary signs; however, we choose to add them linearly.

REFERENCES

- Anderson, D. L. T., and A. E. Gill, 1975: Spin-up of a stratified ocean with application to upwelling. *Deep-Sea Res. Oceanogr. Abstr.*, **22**, 583–596.
- , and R. A. Corry, 1985: Seasonal transport variations in the Florida Current: A model study. *J. Phys. Oceanogr.*, **15**, 773–786.
- Atkinson, C. P., H. L. Bryden, and T. Kanzow, 2008: Ekman transport variability at 26°N in the Atlantic. *Proc. Rapid Climate Change 2008 Annual General Meeting*, Cambridge, United Kingdom.
- Baringer, M. O., and S. L. Garzoli, 2007: Meridional heat transport determined with expendable bathythermographs—Part I: Error estimates from model and hydrographic data. *Deep-Sea Res. I*, **54**, 1390–1401, doi:10.1016/j.dsr.2007.03.011.
- , W. E. Johns, C. S. Meinen, D. Shoosmith, and H. L. Bryden, cited 2008: On the structure of Florida current variability. [Available online at <http://www.noc.soton.ac.uk/rapid/sci/viewabs1.php?keyword1=gwa806>.]
- Barnier, B., 1988: A numerical study on the influence of the mid-Atlantic Ridge on nonlinear first-mode baroclinic Rossby waves generated by seasonal winds. *J. Phys. Oceanogr.*, **18**, 417–433.
- Beal, L. M., J. M. Hummon, E. Williams, O. B. Brown, W. Baringer, and E. J. Kearns, 2008: Five years of Florida Current structure and transport from the Royal Caribbean cruise ship *Explorer of the Seas*. *J. Geophys. Res.*, **113**, C06001, doi:10.1029/2007JC004154.
- Biau, A., C. W. Böning, and J. Getzlaff, 2008: Causes of interannual-decadal variability in the meridional overturning circulation of the midlatitude North Atlantic Ocean. *J. Climate*, **21**, 6599–6615.
- Böning, C. W., C. Dieterich, B. Barnier, and Y. Jia, 2001: Seasonal cycle of meridional heat transport in the subtropical North Atlantic: A model intercomparison in relation to observations near 25°N. *Prog. Oceanogr.*, **48**, 231–253.
- Bryden, H. L., W. E. Johns, and P. M. Saunders, 2005a: Deep western boundary current east of Abaco: Mean structure and transport. *J. Mar. Res.*, **63**, 35–57.
- , H. R. Longworth, and S. A. Cunningham, 2005b: Slowing of the Atlantic meridional overturning circulation at 25°N. *Nature*, **438**, 655–657.
- , A. Mujahid, S. A. Cunningham, and T. Kanzow, 2009: Adjustment of the basin-scale circulation at 26°N to variations in Gulf Stream, deep western boundary current and Ekman transports as observed by the RAPID array. *Ocean Sci.*, **5**, 421–433.
- Cabanes, C., T. Lee, and L.-L. Fu, 2008: Mechanisms of interannual variations of the meridional overturning circulation of the North Atlantic Ocean. *J. Phys. Oceanogr.*, **38**, 467–480.
- Chelton, D. B., M. G. Schlax, M. H. Freilich, and R. F. Milliff, 2004: Satellite measurements reveal persistent small-scale features in ocean winds. *Science*, **303**, 978–983.
- Chidichimo, M. P., T. Kanzow, S. A. Cunningham, and J. Marotzke, 2010: The contribution of eastern-boundary density variations to the Atlantic meridional overturning circulation at 26.5°N. *Ocean Sci.*, **6**, 475–490.
- Cunningham, S. A., and S. Alderson, 2007: Transatlantic temperature and salinity changes at 24.5°N from 1957 to 2004. *Geophys. Res. Lett.*, **34**, L14606, doi:10.1029/2007GL029821.
- , and Coauthors, 2007: Temporal variability of the Atlantic meridional overturning circulation at 26.5°N. *Science*, **317**, 935–938.

- Delworth, T., S. Manabe, and R. J. Stouffer, 1993: Interdecadal variations of the thermohaline circulation in a coupled ocean–atmosphere model. *J. Climate*, **6**, 1993–2011.
- Fennel, W., and H. U. Lass, 2007: On the impact of wind curls on coastal currents. *J. Mar. Syst.*, **68**, 128–142.
- Ganachaud, A., 2003a: Error budget of inverse box models: The North Atlantic. *J. Atmos. Oceanic Technol.*, **20**, 1641–1655.
- , 2003b: Large-scale mass transports, water mass formation, and diffusivities estimated from World Ocean Circulation Experiment (WOCE) hydrographic data. *J. Geophys. Res.*, **108**, 3213, doi:10.1029/2002JC001565.
- Garzoli, S. L., and M. O. Baringer, 2007: Meridional heat transport determined with expandable bathythermographs—Part II: South Atlantic transport. *Deep-Sea Res. I*, **54**, 1402–1420, doi:10.1016/j.dsr.2007.04.013.
- Hall, M. M., and H. L. Bryden, 1982: Direct estimates and mechanisms of ocean heat transport. *Deep-Sea Res.*, **29A**, 339–359.
- Herrmann, P., and W. Krauss, 1989: Generation and propagation of annual Rossby waves in the North Atlantic. *J. Phys. Oceanogr.*, **19**, 727–744.
- Hirschi, J. J.-M., and J. Marotzke, 2007: Reconstructing the meridional overturning circulation from boundary densities and the zonal wind stress. *J. Phys. Oceanogr.*, **37**, 743–763.
- , J. Baehr, J. Marotzke, J. Stark, S. Cunningham, and J.-O. Beismann, 2003: A monitoring design for the Atlantic meridional overturning circulation. *Geophys. Res. Lett.*, **30**, 1413, doi:10.1029/2002GL016776.
- , P. D. Killworth, and J. R. Blundell, 2007: Subannual, seasonal, and interannual variability of the North Atlantic meridional overturning circulation. *J. Phys. Oceanogr.*, **37**, 1246–1265.
- , —, —, and D. Cromwell, 2009: Sea surface height signals as indicators for oceanic meridional mass transports. *J. Phys. Oceanogr.*, **39**, 581–601.
- Houghton, J. T., Y. Ding, D. J. Griggs, M. Noguer, P. J. van der Linden, X. Dai, K. Maskell, and C. A. Johnson, Eds., 2001: *Climate Change 2001: The Scientific Basis*. Cambridge University Press, 881 pp.
- Jayne, S. R., and J. Marotzke, 2001: The dynamics of ocean heat transport variability. *Rev. Geophys.*, **39**, 385–411.
- Johns, W. E., T. Kanzow, and R. Zantopp, 2005: Estimating ocean transports with dynamic height moorings: An application in the Atlantic Deep Western Boundary Current at 26°N. *Deep-Sea Res. I*, **52**, 1542–1567.
- , L. M. Beal, M. O. Baringer, J. R. Molina, S. A. Cunningham, T. Kanzow, and D. Rayner, 2008: Variability of shallow and deep western boundary currents off the Bahamas during 2004–05: Results from the 26°N RAPID–MOC array. *J. Phys. Oceanogr.*, **38**, 605–623.
- Johnson, G. C., and N. Gruber, 2007: Decadal water mass variations along 20°W in the Northeastern Atlantic Ocean. *Prog. Oceanogr.*, **73**, 277–295.
- Joyce, T. M., and P. Robbins, 1996: The long-term hydrographic record at Bermuda. *J. Climate*, **9**, 3121–3131.
- , R. S. Pickart, and R. C. Millard, 1999: Long-term hydrographic changes at 52° and 66°W in the North Atlantic subtropical gyre and Caribbean. *Deep-Sea Res. II*, **46**, 245–278.
- Kalnay, E., and Coauthors, 1996: The NCEP/NCAR 40-Year Reanalysis Project. *Bull. Amer. Meteor. Soc.*, **77**, 437–471.
- Kanzow, T., 2000: Integrale Erfassung langperiodischer Transporte: Simulation und Optimierung eines verankerten Systems. M.S. thesis, Department of Mathematics and Natural Sciences, Christian-Albrechts-University, 95 pp.
- , and M. Visbeck, 2009: Ocean currents as indicator of climate change. *Climate Change: Observed Impacts on Planet Earth*, T. M. Letcher, Ed., Elsevier, 349–366.
- , U. Send, W. Zenk, A. D. Chave, and M. Rhein, 2006: Monitoring the integrated deep meridional flow in the tropical North Atlantic: Long-term performance of a geostrophic array. *Deep-Sea Res. I*, **53**, 528–546.
- , and Coauthors, 2007: Observed flow compensation associated with the MOC at 26.5°N in the Atlantic. *Science*, **317**, 938–941.
- , and Coauthors, 2008a: A prototype system for observing the Atlantic meridional overturning circulation: Scientific basis, measurement and risk mitigation strategies, and first results. *J. Oper. Oceanogr.*, **1**, 19–28.
- , U. Send, and M. McCartney, 2008b: On the variability of the deep meridional transports in the tropical North Atlantic. *Deep-Sea Res. I*, **55**, 1601–1623, doi:10.1016/j.dsr.2008.07.011.
- , H. Johnson, D. Marshall, S. A. Cunningham, J. J.-M. Hirschi, A. Mujahid, H. L. Bryden, and W. E. Johns, 2009: Basinwide integrated volume transports in an eddy-filled ocean. *J. Phys. Oceanogr.*, **39**, 3091–3110.
- Kieke, D., B. Klein, L. Stramma, M. Rhein, and K. P. Koltermann, 2009: Variability and propagation of Labrador Sea Water in the southern subpolar North Atlantic. *Deep-Sea Res. I*, **56**, 1656–1674.
- Killworth, P. D., and J. R. Blundell, 2005: The dispersion relation for planetary waves in the presence of mean flow and topography. Part II: Two-dimensional examples and global results. *J. Phys. Oceanogr.*, **35**, 2110–2133.
- Köhl, A., 2005: Anomalies of meridional overturning: Mechanisms in the North Atlantic. *J. Phys. Oceanogr.*, **35**, 1455–1472.
- Larsen, J. C., 1992: Transport and heat flux of the Florida Current at 27°N derived from cross-stream voltages and profiling data: Theory and observations. *Philos. Trans. Roy. Soc. London*, **338A**, 169–236.
- Latif, M., and Coauthors, 2004: Reconstructing, monitoring, and predicting multidecadal-scale changes in the North Atlantic thermohaline circulation with sea surface temperature. *J. Climate*, **17**, 1605–1614.
- Lee, T., cited 2009: Consistency of AMOC estimates from global ocean data assimilation (ODA) products. [Available online at <http://www.atlanticmoc.org/AMOC2009agenda.php>.]
- Lee, T. N., W. E. Johns, R. J. Zantopp, and E. R. Fillenbaum, 1996: Moored observations of western boundary current variability and thermocline circulation at 26.5°N in the subtropical North Atlantic. *J. Phys. Oceanogr.*, **26**, 962–983.
- Levitus, S., 1982: *Climatological Atlas of the World Ocean*. NOAA Prof. Paper 13, 173 pp. and 17 microfiche.
- Longworth, H. R., 2007: Constraining variability of the Atlantic meridional overturning circulation at 26.5°N from historical observations. Ph.D. thesis, University of Southampton, 198 pp.
- Lumpkin, R., and K. Speer, 2007: Global ocean meridional overturning. *J. Phys. Oceanogr.*, **37**, 2550–2562.
- McCartney, M. S., and R. A. Curry, 1993: Transequatorial flow of Antarctic bottom water in the western Atlantic Ocean: Abyssal geostrophy at the equator. *J. Phys. Oceanogr.*, **23**, 1264–1276.
- Meinen, C. S., M. O. Baringer, and R. F. Garcia, 2010: Florida Current transport variability: An analysis of annual and longer-period signals. *Deep-Sea Res. I*, **57**, 835–846, doi:10.1016/j.dsr.2010.04.001.

- Mercier, H., and K. Speer, 1998: Transport of bottom water in the Romanche Fracture Zone and Chain Fracture Zone. *J. Phys. Oceanogr.*, **28**, 779–790.
- Orsi, A. H., W. M. Smethie Jr., and J. L. Bullister, 2002: On the total input of Antarctic waters to the deep ocean: A preliminary estimate from chlorofluorocarbon measurements. *J. Geophys. Res.*, **107**, 3122, doi:10.1029/2001JC000976.
- Osychny, V., and P. Cornillon, 2004: Properties of Rossby waves in the North Atlantic estimated from satellite data. *J. Phys. Oceanogr.*, **34**, 61–76.
- Risien, C. M., and D. B. Chelton, 2008: A global climatology of surface wind and wind stress fields from eight years of QuikSCAT scatterometer data. *J. Phys. Oceanogr.*, **38**, 2379–2413.
- Roemmich, D., and C. Wunsch, 1985: Two transatlantic sections: Meridional circulation and heat flux in the subtropical North Atlantic Ocean. *Deep-Sea Res.*, **32**, 619.
- Schlax, M. G., D. B. Chelton, and M. H. Freilich, 2001: Sampling errors in wind fields constructed from single and tandem scatterometer datasets. *J. Atmos. Oceanic Technol.*, **18**, 1014–1036.
- Schott, F. A., J. Fischer, M. Dengler, and R. Zantopp, 2006: Variability of the deep western boundary current east of the Grand Banks. *Geophys. Res. Lett.*, **33**, L21S07, doi:10.1029/2006GL026563.
- Smith, G. C., K. Haines, T. Kanzow, and S. Cunningham, 2009: Impact of hydrographic data assimilation on the Atlantic meridional overturning circulation. *Ocean Sci. Discuss.*, **6**, 2667–2715, doi:10.5194/osd-6-2667-2009.
- Sturges, W., B. G. Hong, and A. J. Clarke, 1998: Decadal wind forcing of the North Atlantic subtropical gyre. *J. Phys. Oceanogr.*, **28**, 659–668.
- Talley, L. D., J. L. Reid, and P. E. Robbins, 2003: Data-based meridional overturning streamfunctions for the global ocean. *J. Climate*, **16**, 3213–3226.
- Tennekes, H., and J. L. Lumley, 1972: *A First Course in Turbulence*. The MIT Press, 300 pp.
- Wijffels, S. E., 2001: Ocean transport of fresh water. *Ocean Circulation and Climate: Observing and Modelling the Global Ocean*, G. Siedler, J. Church, and J. Gould, Eds., International Geophysics Series, Vol. 77, Academic Press, 475–488.
- Woodgate, R. A., and K. Aagaard, 2005: Revising the Bering Strait freshwater flux into the Arctic Ocean. *Geophys. Res. Lett.*, **32**, L02602, doi:10.1029/2004/GL021747.
- Wunsch, C., and P. Heimbach, 2009: The globally integrated ocean circulation (MOC), 1992–2006: Seasonal and decadal variability. *J. Phys. Oceanogr.*, **39**, 351–368.